AN ABSTRACT OF THE THESIS OF

Moira H. Meek for the degree of Master of Science in Civil Engineering presented on June 08, 2023

Title: Hydrodynamic Modeling of Submerged Wave Energy Converters: Power Take-Off Mooring Configuration Effect on Power Performance

Abstract approved:

Bryson Robertson

Wave energy converters (WECs) show promising potential to significantly contribute to global renewable energy goals. Numerous WEC designs have been proposed and investigated, but wave energy conversion technology has yet to reach convergence in the same way wind or solar has. Of the designs currently in existence, surface-piercing WECs are the most prevalent, and subsurface WECs are only in the beginning stages of gaining a foothold in the space. However, there are distinct advantages of subsurface WECs that make them a compelling pursuit, including increased resiliency to extreme wave conditions and the ability to submerge them within the water column so as to create no surface expression or to deconflict with marine traffic. Several subsurface point absorber WEC projects have been initiated by AWS Ocean Energy, Symphony Wave Power, Carnegie Clean Energy, and CalWave Power Technologies, and have reached later stages of development. However, even within this one WEC archetype, there is non-convergence in their design in regard to their choice of power take-off (PTO) and mooring system configuration. Current research shows that the number of tethers and their configuration in a mooring system affects the dynamics of the WEC and its ability to capture energy in modes of heave, surge, and pitch that can

be converted into usable energy by the PTO system.

This study explores different PTO and mooring system configurations in regular and irregular wave conditions to investigate the effect of increasing the number of tethers and PTOs on power performance. Additionally, the rate of energy generation decay of different configurations is analyzed as they are submerged deeper within the water column. This investigation numerically analyzes a single-tether, three-tether, four-tether, and five-tether configuration in a singular cohesive study utilizing hydrodynamic modeling in ProteusDS, a time-domain dynamics analysis software.

Results suggest that a three-tether system can provide better broadband performance, slightly improved power quality, and reduced PTO damping and tether tension loads over a single-tether configuration but at the cost of adding expenditures and complexity associated with two additional PTOs and supplementary mooring components. Findings also suggest that a three-tether configuration most efficiently utilizes its energy capture modes, and adding additional tethers and PTOs does not result in a significant benefit and may actually lead to less energy generation. All configurations are shown to have similar energy generation decay that follows the exponential decaying trends of the wave orbital trajectories.

Hydrodynamic Modeling of Submerged Wave Energy Converters: Power Take-Off Mooring Configuration Effect on Power Performance

by
Moira H. Meek

A THESIS

submitted to

Oregon State University

in partial fulfillment of
the requirements for the
degree of

Master of Science

Presented June 08, 2023
Commencement June 2023

Master of Science thesis of Moira H. Meek presented on June 08, 2023.

APPROVED:

Major Professor, representing Civil Engineering

Head of the School of Civil and Construction Engineering

Dean of the Graduate School

I understand that my thesis will become part of the permanent collection of Oregon State University libraries. My signature below authorizes release of my thesis to any reader upon request.

Moira H. Meek, Author

ACKNOWLEDGEMENTS

Thank you to all those who have supported me throughout this journey to graduate school, and in this particular endeavor. My family, who has seen me through it all, from providing me the upbringing that allowed me to study at the Coast Guard Academy, to two afloat tours, and now completion of graduate school. I also would like to express my sincere gratitude for my friends, both scattered across the country and the ones made here in my time in Corvallis that have been there for me in the most amazing ways. And finally, thank you to the Coast Guard and my shipmates that have given me the opportunity to study Ocean Engineering at Oregon State and provided me the mentorship and fellowship to grow professionally and continue to absolutely love my job. Looking forward to see where this next assignment in Juneau takes me, and forever grateful for the knowledge, friendship, and fun I've had here in Oregon.

TABLE OF CONTENTS

TABLE OF CONTENTS (Continued)

Page

LIST OF FIGURES

LIST OF TABLES

Chapter 1

Introduction

Wave power is concentrated near the surface. In fact, 95% of the energy is located between the water surface and a depth of one-fourth of the wavelength. The greatest potential is also located offshore, in medium-high latitudes between 30° and 60° latitudes, and in water depths greater than 40 meters where power densities reach 60-70 kilowatts per meter [1, 2]. A map of the global offshore average annual wave power distribution is depicted in Figure 1.1.

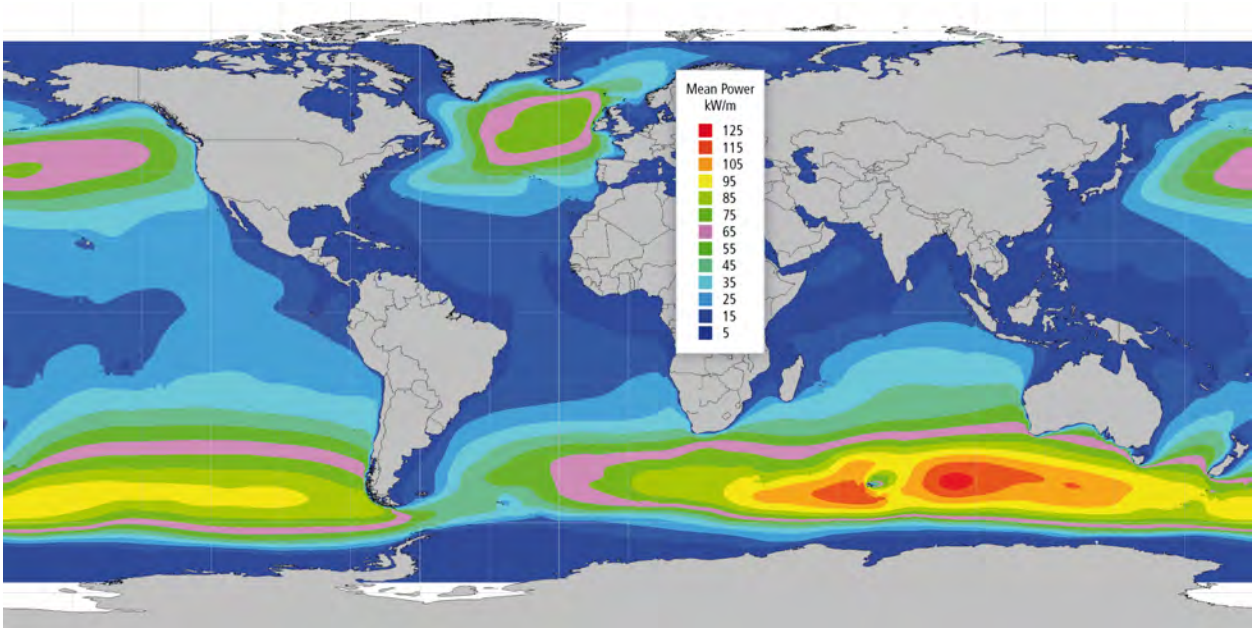

Figure 1.1: Global offshore annual wave power level distribution [3].

However, to take advantage of the most attractive locations for wave power, wave energy converters (WECs) must have the ability to withstand the extreme wave conditions that exist there. There are over 1000 patented WEC designs, ranging from conceptual to commercialized devices [4]. Surface-piercing WECs are the most prevalent, but their designs are

often not compatible to be moored at the depths in these regions, and if capable they are vulnerable to damage or subject to working limits that curb their operational time. In contrast, subsurface WECs have an inherent resiliency to extreme sea states in their placement below the surface. This thesis explores subsurface WECs as an alternative to surface-piercing WECs to capture the vast offshore wave resource while prevailing against the immense power of the sea. The main objective of this thesis is to answer two research questions regarding subsurface WECs:

RESEARCH QUESTION 1 (RQ1). How does the number of tethers in a coupled power take-off mooring system affect power performance in a subsurface WEC?

RESEARCH QUESTION 2 (RQ2). How does the energy generation decay with increasing submergence depths for WECs with different mooring system configurations?

To answer these questions, four different configurations of a submerged WEC are modeled: single-tether, three-tether, four-tether, and five-tether configurations, illustrated in Figure 1.2.

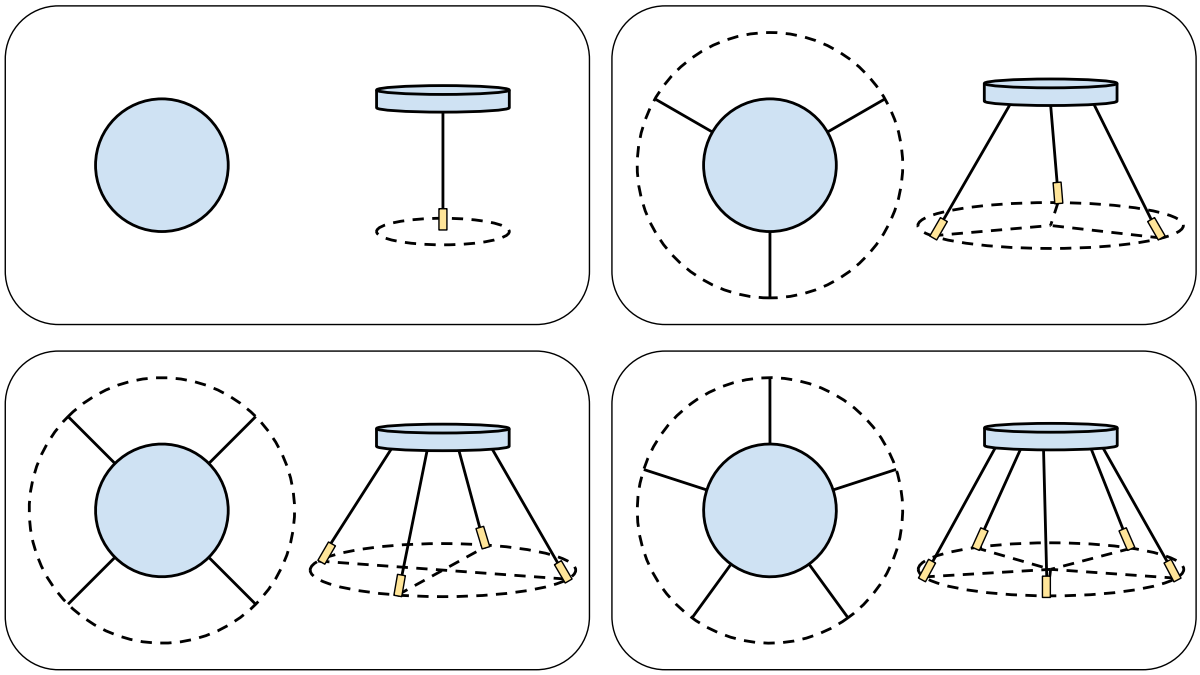

Figure 1.2: Artistic rendering of the four coupled power take-off mooring system configurations with orthographic and top views.

For RQ1, their response in both regular and irregular wave conditions is analyzed to

assess their power performance in deep water conditions. Metrics for power performance include energy generation, coefficient of variation of the instantaneous power, capture width ratio, and tether tension. The aim of RQ1 is to gain a better understanding of how increasing the number of tethers affects energy generation, the contribution of different modes to energy capture, and power quality. For RQ2, the same four configurations are analyzed at different submergence depths of the hydrodynamic body while keeping other design parameters the same. The aim of RQ2 is to gain a better understanding of how mooring configuration affects energy generation decay and their relationship to the decay rates of wave orbital trajectories. This analysis is visualized in Figure 1.3.

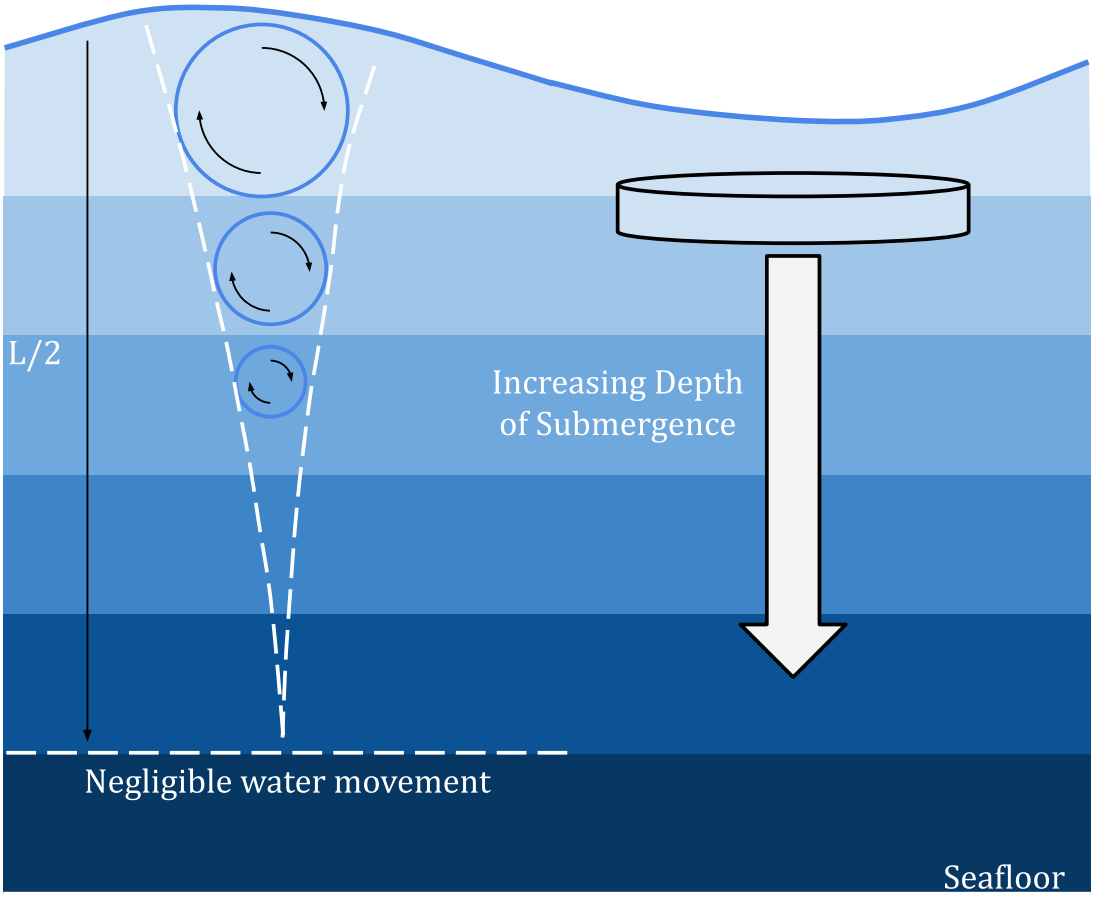

Figure 1.3: Illustration of the energy decay analysis with wave orbital decay.

To provide consistency and clarity, the following terminology used throughout this document is delineated below:

- **Configuration**: the geometric arrangement of the mooring system's tether(s)
- **Tether**: a physical cable or mooring line

- **Mooring System**: the components that station keep the WEC which may consist of a single tether or multiple tethers
- **Power Take-off (PTO)**: the system that WECs use to capture the power of waves that converts mechanical power into electricity
- **Coupled PTO-mooring system**: a mooring system in which a PTO is associated with each tether (i.e. the number of tethers equals the number of PTOs in the system)
- **Hydrodynamic body**: a component of the WEC that is interacting with and being excited by the waves for the purpose of energy capture
- **Modes**: motion of the hydrodynamic body in heave, surge, and pitch that contribute to WEC energy capture
- **Depth of Submergence**: the distance the hydrodynamic body is in the water column from the still water line

Motivation

Subsurface WECs have not been well explored in comparison to surface-piercing WECs. This is primarily due to the wave energy decay with depth, and the energy generation potential being prioritized in WEC design. However, there are distinct advantages of subsurface WECs over their surface-piercing counterparts that make them a compelling solution. With their submerged nature protecting them from extreme sea states they can bypass the need to overengineer structures or incorporate a survival mode system. There are also several reasons to desire a subsurface over a surface-piercing design regarding their placement in the water column, whether to minimize visual impact, a requirement for no surface expression, or to submerge the system deeper so as to not impede marine traffic.

Subsurface WECs are emerging in the wave energy technology space, and several well-established companies have put forth submerged WEC designs, AWS Ocean Energy's Archimedes Wave Swing [5], Symphony Wave Power's Symphony WEC [6], Carnegie Clean Energy's CETO 6 [7], and CalWave's xWave [8]. Images of these WECs are shown in Figure 1.4. The four aforementioned WECs capture wave energy using the same basic underlying principle, yet each company has opted for contrasting float geometries, varied mooring systems, and different design submergence depths. There is a lack of consensus on the justification for these design choices, and this thesis investigates the trade-offs of increasing the number of tethers and the implications of the submergence depth of the hydrodynamic body.

This research focuses on the hydrodynamic modeling of submerged wave energy converters, and numerical analysis and comparison. While purely numerical, this work intends to support the build of a prototype submerged point absorber for experimental testing in the O.H. Hinsdale Wave Research Laboratory located at Oregon State University. The results

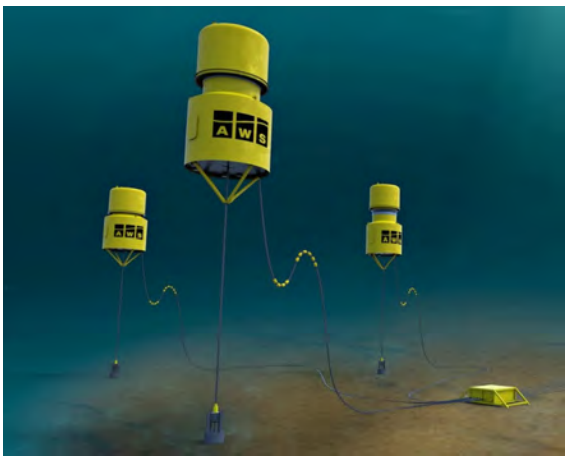

(a) AWS Ocean Energy's AWS [9].

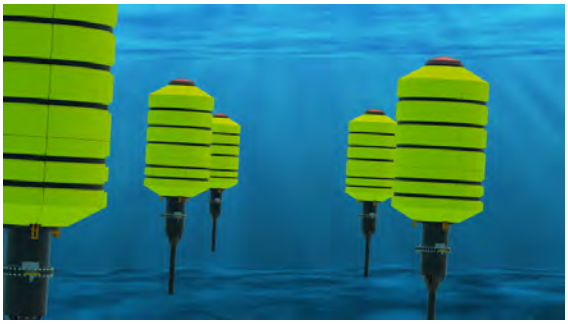

(b) Symphony Wave Power's Symphony WEC [10]

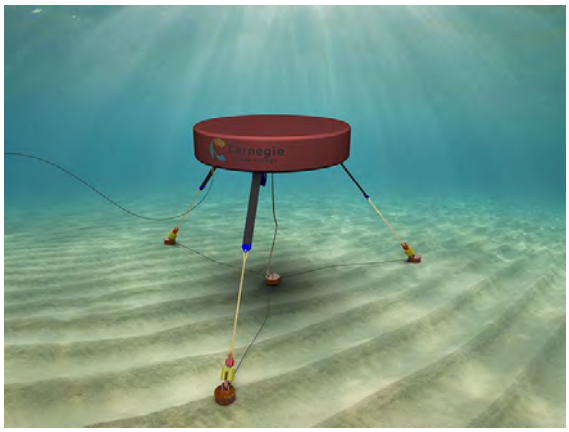

(c) Carnegie Clean Energy's CETO 6 [11].

(d) CalWave's xWave [12].

Figure 1.4: Submerged Point Absorber WEC designs.

of this study seek to inform design choices for the physical model. The methods and tools that are presented have been created to apply to WECs other than the specific case study examined in this thesis. The broader goals of this work are to establish methods to model subsurface WECs which have specific nuances, especially concerning the PTO, that make them more complex within the constraints of the modeling software, and to discover trends in behavior with adding additional tethers or increased submergence depth. Specific values found in the analysis have caveats associated with them. However, the systematic approach to modeling each configuration is designed to allow reasonable comparison between configurations and create a starting point from which to continue analysis with increased fidelity modeling techniques.

Thesis Outline

Chapter 2, reviews the current status of subsurface WEC technology, relevant submerged point absorber research, and research gaps. Chapter 3, provides background knowledge

on wave models, WEC hydrodynamics, and the ProteusDS modeling software. Chapter 4 outlines ProteusDS WEC modeling and details the analysis methods. Chapter 5, establishes the specifics of the WEC used as a case study, provides the modeling setup in ProteusDS, and outlines the wave conditions used. Chapter 6, presents the results of the ProteusDS simulations of the WEC case study and calculations of the performance metrics. Chapter 7, provides further explanation of observations from the results, and limitations of this study. Finally, Chapter 8, summarizes this research, the impact of findings, and proposed future work.

Chapter 2

Background

The following sections provide background knowledge that is drawn upon in other portions of this thesis. Section 2.1 outlines relevant theory on wave models used in this study. Section 2.2 provides a breakdown of the WEC hydrodynamics, focusing on the time-domain equation of motion, and details its components. Section 2.3, gives an overview of the capabilities and application of the ProteusDS software that is used for numerical modeling and simulations. Table 2.1 lists common notation used throughout this chapter.

Symbol	Definition
η	Wave surface elevation
H	Wave height [m]
T	Wave period [s]
ω	Wave angular frequency [rad/s]
k	wave number [1/m]
θ	Wave direction [deg]
ϕ	Wave phase [rad]
L	Wave length [m]
h	Water depth [m]
g	Gravitational acceleration [m/s^2]
ρ	Water density [kg/m^3]
H_s	Significant wave height [m]
ω_p	Peak wave frequency [Hz]
T_p	Peak wave period [s]
T_e	Wave energy period [s]

Table 2.1: Common notation used throughout this section.

2.1 Wave Models

An Airy wave model, based on a linear theory, is commonly used to model regular waves which are composed of a single wave component defined by wave direction, height, and period [13]. This wave model results in a long-crested swell with only one dominant frequency and is formulated as a single, repeating sinusoidal. The incident wave is defined with Equation 2.1 [14].

$$\eta(x, y, t) = \frac{H}{2} \cos \omega t - k(x \cos \theta + y \sin \theta + \phi) \tag{2.1}$$

the wave number is $k = 2\pi/L$, but often is calculated from the dispersion relation when the water depth and wave period are known. The dispersion relation ties the relationship between the wave angular frequency and wave number (in effect the wavelength) [14]. The full derivation is not included here, but the wave number can be computed iteratively from the dispersion relation, shown in Equation 2.2 [15].

$$\omega^2 = gk \tanh kh \tag{2.2}$$

For regular waves, the wave power in deep water, J_{reg} (in watts per meter), is calculated with Equation 2.3 [16, 17].

$$J_{reg} = \frac{\rho g^2}{32\pi} H^2 T \tag{2.3}$$

In a regular wave, the shape of water particle trajectories changes with relative water depth. Relative water depth is determined by the ratio of water depth to wavelength and is categorized into deep water ($h/L > 1/2$), intermediate water ($1/20 < h/L < 1/2$), and shallow water ($h/L < 1/20$). These water particle kinematics, along with the pressure field within the waves, are directly tied to the forces acting on bodies [18].

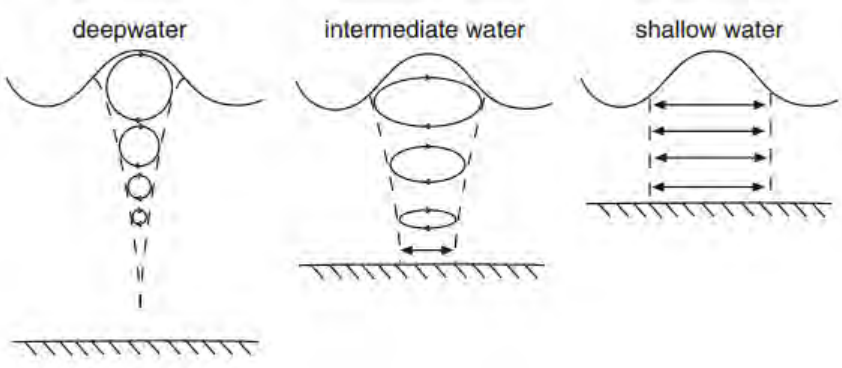

Figure 2.1: Illustration of the orbital motion of Airy waves in deep, intermediate, and shallow water [19].

For deep water waves, water particle trajectories are circles that decay exponentially with depth. At a depth of half the wavelength, the radii of trajectories are only 4% of surface values [18]. The radius of the water particle trajectories in deep water can be calculated with Equation 2.4 and are defined by the wave height, wave number, and the vertical distance from the still water line (z).

$$A = B = \frac{H}{2} e^{kz} \tag{2.4}$$

where A and B are the semi-axes of an ellipse, but in the case of deep water they are equal, meaning they are circular. In deep water, the energy in the wave is equally composed of potential energy (controlled by wave height), and kinetic energy (dependent on the motion of the wave particles) [20]. Therefore, the exponential decay of water particle trajectories is directly tied to a reduction in wave energy further down in the water column. This aspect is a major factor when considering submerged WECs.

A Pierson-Moskowitz (PM) or JOint North Sea WAve Project (JONSWAP) spectrum are commonly used irregular wave models [14, 15]. They have more complex formulations but are more representative of actual sea states, unlike regular waves. The PM spectrum, $S_{PM}(\omega)$, and the JONSWAP spectrum, $S_J(\omega)$, is defined by Equation 2.6 and Equation 2.5, respectively [15].

$$S_{PM}(\omega) = \frac{5}{16} {H_s}^2 {\omega_p}^4 \omega^{-5} exp\left[-\frac{5}{4}\left(\frac{\omega}{\omega_p}\right)^{-4}\right] \tag{2.5}$$

$$S_J(\omega) = A_\gamma S_{PM}(\omega) \gamma^{exp\left(-0.5\left[\frac{\omega-\omega_p}{\sigma\omega_p}\right]^2\right)} \tag{2.6}$$

where γ is the peak shape constant, A_γ is a normalizing parameter ($A_\gamma = 1 - 0.287 \ln \gamma$), and σ is the spectral width parameter ($\sigma = 0.07$ for $\omega \leq \omega_p$, and $\sigma = 0.09$ for $\omega > \omega_p$).

For irregular waves, the wave power, J_{irr} (in watts per meter), is calculated with Equation 2.7 using T_p [16, 17].

$$J_{irr} = \frac{\rho g^2}{64\pi} H_s^2 T_p \tag{2.7}$$

The peak period is related to the energy period by a calibration coefficient α as shown in Equation 2.8.

$$T_e = \alpha T_p \tag{2.8}$$

For a PM spectrum $\alpha = 0.86$ and for a JONSWAP spectrum, assuming a standard peak shape constant of $\gamma = 3.3$, $\alpha = 0.9$ [21, 22].

The decision to use a PM or JONSWAP model is based on the wave climate to be modeled. A PM spectrum is based on the assumption of a fully developed sea, where equilibrium has been reached between the waves and wind. The JONSWAP spectrum is a refinement of the PM spectrum for a developing sea, where equilibrium has not been reached [13]. A PM spectrum is often employed to model wave climates in the Pacific Ocean as it has large areas of uninterrupted fetch, while the JONSWAP spectrum is often preferred to model areas that are fetch limited and more commonly found in the Atlantic Ocean [23].

2.2 WEC Hydrodynamics

From Newton's second law of motion and the original Cummins equation formulation [24], the general force-balance equation for a WEC is shown in Equation 2.9.

$$m\ddot{X} = F_{exc} + F_{rad} + F_{HS} + F_{visc} + F_m + F_{PTO} \tag{2.9}$$

where m is the mass matrix, and the $\ddot{X}$ is the body acceleration. The remaining terms are further defined below.

Wave Excitation Force (F_{exe}) is composed of the *Froude-Krylov force* and *diffraction force*. The excitation force is the force acting on the body due to the incident wave. The *Froude-Krylov* force considers the unsteady pressure field of an undisturbed wave assuming the body is absent, while the *diffraction force* considers the alteration of the wave field due to the presence of the body [25].

Wave Radiation Force (F_{rad}) is the force caused by the displacement of water around the body when the body moves. This force is generally divided into an *added mass force* and a *wave radiation damping force*, which are both frequency dependent. The *added mass force* relates to the inertia force required to accelerate the mass of the surrounding fluid affected by the body's motion. The *wave radiation damping force* relates to the average power exchange between the sea and the body arising from the outgoing waves generated when the body moves [13].

Hydrostatic Restoring Force (F_{HS}) is from the hydrostatic pressure of the fluid acting on the wetted surface of the body, for a fully submerged body this is equal to the force of buoyancy [26].

Viscous Damping Force (F_{visc}) is the resistive force acting on the body by the fluid, due to the fluid's tendency to withstand deformation [27].

Mooring Force (F_m) is the force resulting from the reaction loads applied by cables attached to the body. The force that a cable imparts is a result of elastic deformations and external loading [15].

PTO Force (F_{PTO}) is dependent on the type of PTO system used. A popular starting point for control is representing the system as a simple spring-damper system in which the PTO force is composed of two components, one proportional to velocity which is a damping force (purely resistive), and one proportional to displacement which is a spring force [14].

2.3 ProteusDS

ProteusDS is a time-domain dynamics analysis software package developed by Dynamic Systems Analysis Ltd. (DSA) that is used to model marine, offshore, and subsea systems and technologies, including WECs. This software is commonly used to determine system response to environmental conditions such as waves, winds, and currents [15]. The coordinate frame convention is positive x aligned with 0° North, positive y aligned with 90° East, and positive z down towards the seabed [28]. Figure 2.2 illustrates this coordinate frame convention and the directions of translational and rotational degrees of freedom (DoF).

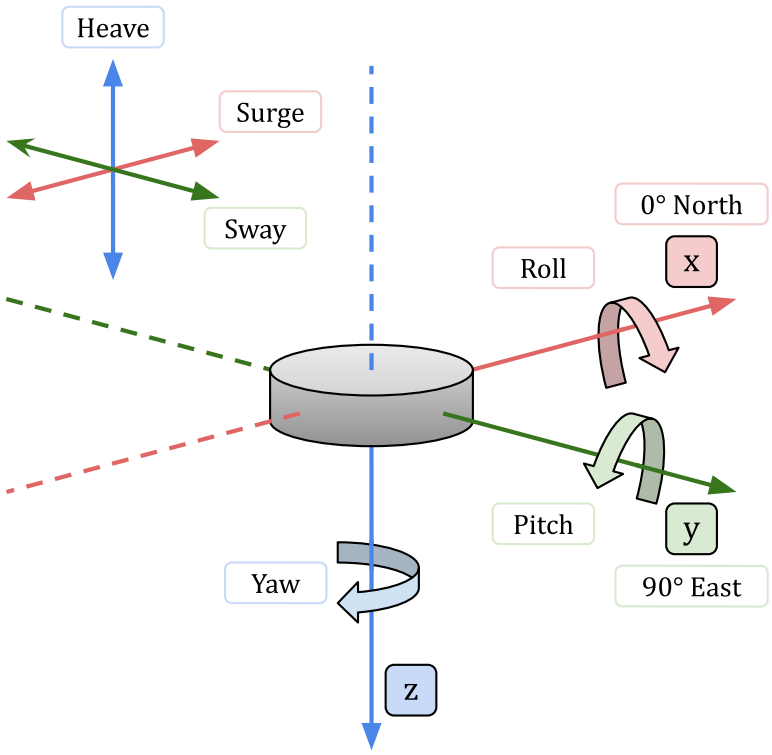

Figure 2.2: ProteusDS coordinate frame.

ProteusDS can model WEC hydrodynamic bodies, and mooring systems with rigid bodies and cables. Rigid bodies and cables are generated in ProteusDS as dynamic objects

(DObjects). Physical parameters and features are assigned to DObjects to give them characteristics. Connections between DObjects can also be made [15]. The power take-off (PTO) system can be modeled with an articulated body algorithm (ABA) joint between two rigid bodies, the nuances of which are further elaborated on in the Methodology. The relevant components used to model WECs in ProteusDS are defined below.

Dynamic Objects.

Rigid Body Used to model vessels, buoys, mechanisms, or any rigid body with mass and inertia free to move with translational and rotational motion [28].

Dynamic Cable Used to simulate flexible structures such as moorings or ropes. Uses a cubic-spline lumped mass cable model. Cable ends are defined in terms of nodes 0/N [15].

Static Cable Used to model a single-element line. It is often useful for representing springs or short stiff lines [28]. If there is an expected catenary or significant distributed load in the cable a static cable should not be used [29].

Each DObject has an associated input file and data file. The input file contains mass, mass moments of inertia, center of gravity (CG) positions, and a reference to features that the DObject uses. The data file contains information about the DObject's state. The state of a DObject may be its initial position, velocity, and orientation, or for an ABA joint connected follower DObject, the joint's initial position, and velocity [15].

Features.

Rigid Body Cylinder Defines cylinder dimensions and mesh parameters for hydrodynamic loading. Utilizes a mesh-based Morison hydrodynamics model. It models added mass, drag and buoyancy, and incident wave loading acting on the submerged portions of the model [28].

Dynamic Cable Segment Defines mechanical and hydrodynamic properties for cable segments such as diameter, axial rigidity, bending rigidity, and torsional rigidity [28].

Rigid Body Linear Quadratic Drag Defines constant linear and quadratic drag/damping loading that is dependent on relative velocity. The feature may be added to a RigidBody. Linear damping is proportional to the velocity, and quadratic damping is proportional to the square of velocity [28].

Rigid Body ABA Connection Joint Defines the joint properties for ABA connections, such as joint stiffness, damping, and end stop locations [28].

More than one DObject can reference the same feature, and a single DObject may reference several features to fully define its characteristics and dynamics [15].

Connections.

Point Connection Connects a Cable end to a fixed point relative to the Rigid Body's frame. The boundary end node state of position and velocity is computed by the Rigid Body and a reaction load from the boundary node is applied to the Rigid Body [28].

ABA Connection Creates an articulated rigid body joint between two rigid bodies. Depending on the chosen joint type, this constrains the relative motion between the two rigid bodies. Common types include prismatic and spherical joints [28].

Each connection is defined in terms of a master DObject and a follower DObject. ProteusDS places restrictions on what DObjects can be connected together and which roles they can have. For instance, ABA connections can only be between two rigid bodies, and a single rigid body cannot be the follower for more than one DObject. Cables can be connected to a rigid body with a point connection, but they must be the follower [15].

Every ProteusDS model is built in the ProteusDS Simulation Toolbox. Simulations are run from the compilation of files that are generated from the Simulation Toolbox graphical user interface (GUI). The GUI is split into sections: Environment, Simulation, Library, Connections, and DObjects which is further sectioned into Rigid Bodies and Cables. The Environment section contains settings for wave ramp up time, water depth, and wave model input. The wave models available in ProteusDS include Airy waves, PM, and JONSWAP spectrums [29]. The Simulation section contains settings for the time interval output, simulation time, and integrator type. The standard numerical integrator is an adaptive 4th/5th Runge-Kutta (Explicit) which includes parameters to set error tolerance, initial time step size, and maximum and minimum time steps. It is one of the most stable and accurate explicit integrators and is recommended for most simulations. When high-frequency dynamics are present, the time step adapts to avoid destabilization [29]. The Library section contains all the features that are used in the simulation, and the Connections section contains all the connections between DObjects.

An illustration of how ProteusDS organizes input data, and some of the ways the DObjects, features, and connections relate to each other is depicted in Figure 2.3, supposing the following DObjects: (1) float, (2) tether, (3) PTO component one, and (4) PTO component two. This figure is only an example and other links exist between entities in a fully developed model.

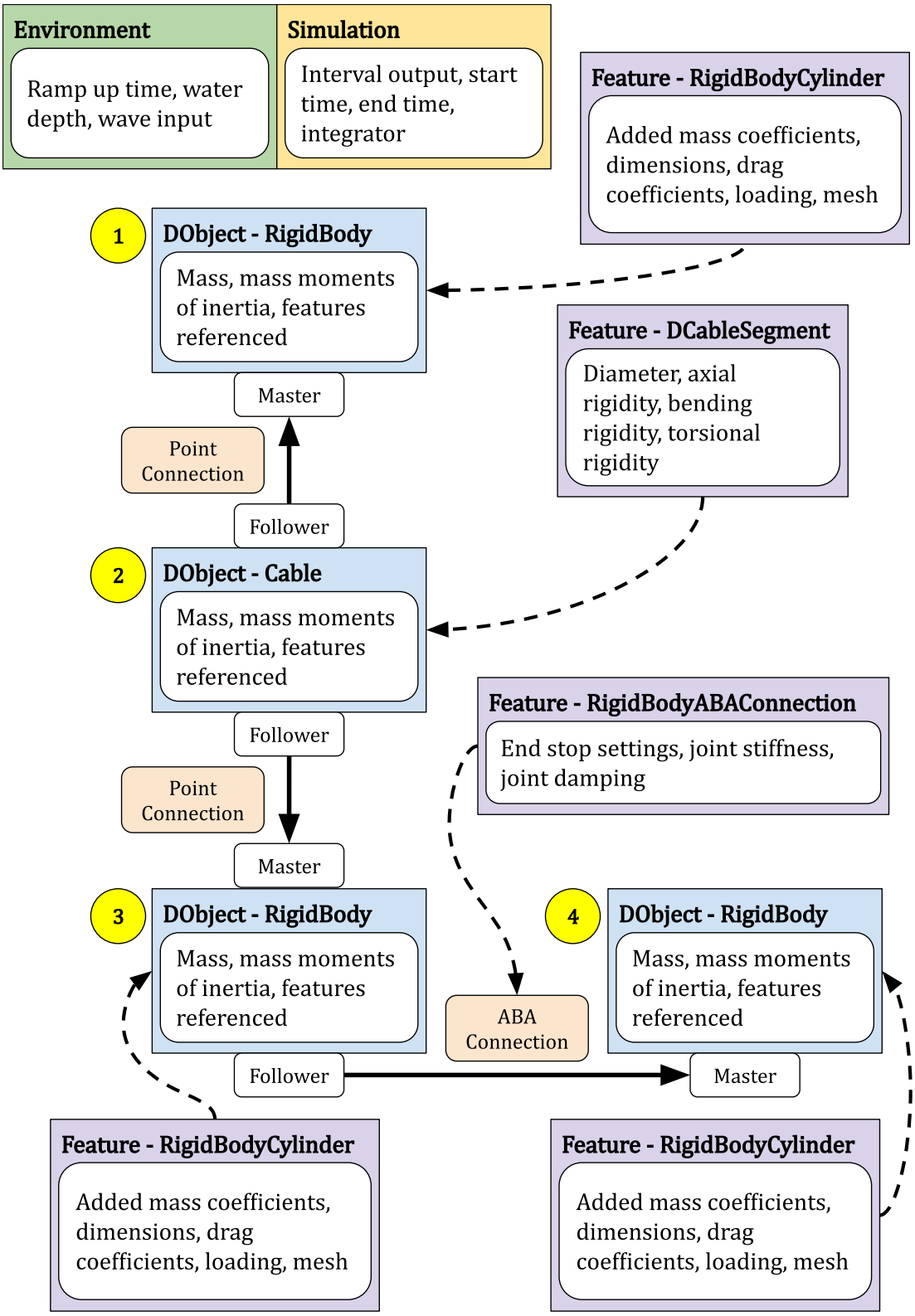

Figure 2.3: Example of the organization and relationships in ProteusDS.

In this diagram, the following key is used:

Green = Environment section

Light Yellow = Simulation section

Blue = DObject section

Purple = Library section

Light Orange = Connections section

Solid Arrows = connections between DObjects pointing from the follower DObject to the master DObject

Curved Dashed Arrows = referenced features of the entity it points to

ProteusDS provides output data, the most relevant of which is position and velocity data for rigid bodies, and tension values for cables. In ProteusDS, position data output is in regards to the global reference frame in terms x, y, z, ϕ (roll angle), θ (pitch angle), and ψ (heading angle) [15]. Additional coordinate transformation is conducted to determine body responses in surge, heave, and pitch in terms of its local reference frame. Velocity data output is in regards to the rigid body local reference frame in terms of linear velocities u, v, and w, and angular components p, q, and r [15]. The velocity of all rigid bodies is directly taken from this output and used in calculations and analysis. Tension data for cables are output for each element.

The two aforementioned models used for cables and rigid body features, the cubic-spline lumped mass cable model and the mesh-based Morison hydrodynamics model that ProteusDS utilizes are now summarized. Proteus discretizes cables into N lumped mass nodes, meaning mass is lumped at the element nodes. The curvature values, needed to calculate flexural response, are determined by fitting a cubic spline through the node points. The internal reaction forces are dictated by Newton's second law of motion and are due to bending, axial and torsional strains. Hydrodynamic loading is assumed to vary linearly along the cable with the distributed load evaluated at the node points following the same Morison load approach used for rigid bodies [15].

ProteusDS' Morison load approach utilizes Morison's hypothesis that the forces acting on a submerged body moving relative to a fluid can be represented as the sum of drag and inertial forces. This includes the drag force, Froude-Krylov force, and added mass force (inertial force) [15]. ProteusDS calculates the Froude-Krylov force using the discretized mesh of a rigid body, defined in its rigid body feature, to calculate the pressure of the fluid on each face. The drag force is calculated with Equation 2.10 [15].

$$F_d = \frac{1}{2}\rho C_d A_{proj} v^2 \tag{2.10}$$

where C_d is the drag coefficient, A_{proj} is the frontal projected area in the direction of the relative fluid flow, and v is the relative fluid velocity. C_d values are found empirically, but can be estimated for simple geometries using values from literature [15]. The C_d values are

set in ProteusDS in the rigid body feature and are nondimensional values. The added mass force is calculated using added mass coefficients which are also defined in the rigid body feature. Added mass coefficients for Morison's approach are well established in the literature for simple shapes [15]. In addition, a Rigid Body Linear Quadratic Drag feature can be added to a rigid body to apply linear and quadratic damping using matrices that have units of Ns/m or Ns^2/m^2, respectively.

Finally, Figure 2.4 ties ProteusDS back to the equation of motion shown in Equation 2.9 and shows where each component is accounted for.

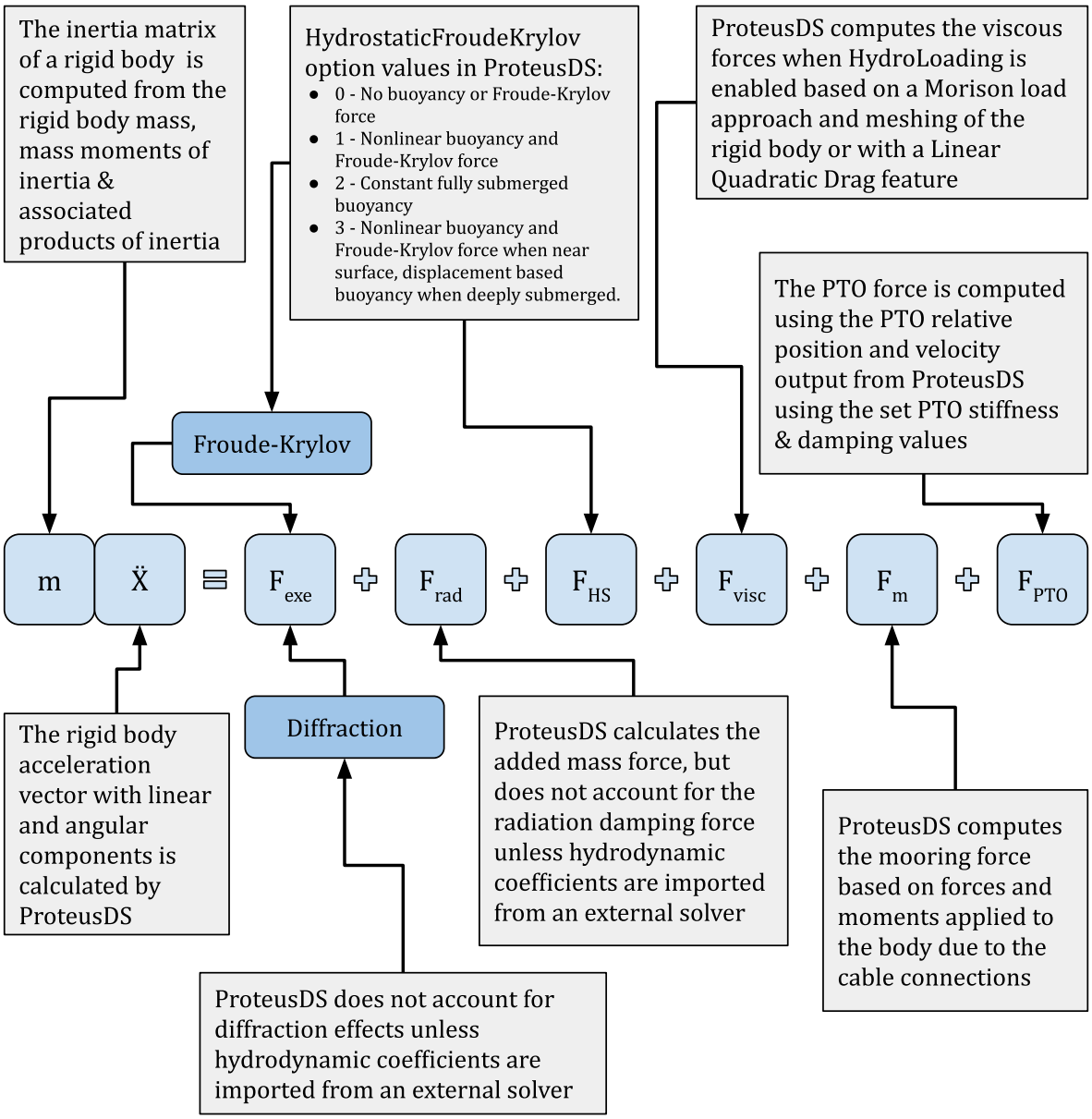

Figure 2.4: ProteusDS' equation of motion breakdown.

Chapter 3

Literature Review

Wave energy conversion technology dates back to 1799 with the first technique patented by Girard & Son in France [30]. Since its inception, wave energy research, and development has had a fluctuation in interest largely driven by fossil fuel markets and the global prioritization of carbon emission reduction. Over the decades, theoretical background and WEC conversion principles have been generally established, but WEC technology has yet to reach convergence. This non-convergence creates a barrier in terms of comparing their performance or efficiencies and moving the technology forward to match the maturity of other renewable energy technologies such as wind and solar. The majority of early and current WEC research focuses on surface-piercing designs, while subsurface has only risen more recently in the wave energy space. Section 3.1 outlines historical classifications of WEC technology. Section 3.2 goes into detail on major developments in submerged WEC technology broken out by archetype. Finally, 3.3 reviews current research specifically regarding submerged point absorbers and identifies research gaps.

3.1 WEC Technology Classifications

Several wave energy technology reviews have been published over the years, but often slightly vary in their delineations or sub-categorizations. Budal and Falnes initiated classification by orientation in 1975, defining four main categories: terminators, attenuators, point absorbers, and quasi-point absorbers [31]. These classifications are illustrated in Figure 3.1.

Classification by orientation.

A *terminator* lies perpendicular to the predominant wave direction and can be described as intercepting the waves [32].

A *attenuator* lies parallel to the predominant wave direction and can be described as "riding" the waves in the case of floating bodies [32].

A *point absorber* is small in characteristic dimension relative to the incident wavelength, and generally axisymmetric so as to be able to absorb power regardless of the predominant wave direction [33].

A *quasi-point absorber* an axisymmetric WEC, insensitive to wave direction similar to a point absorber, but has relatively large dimensions compared with the wavelength [33].

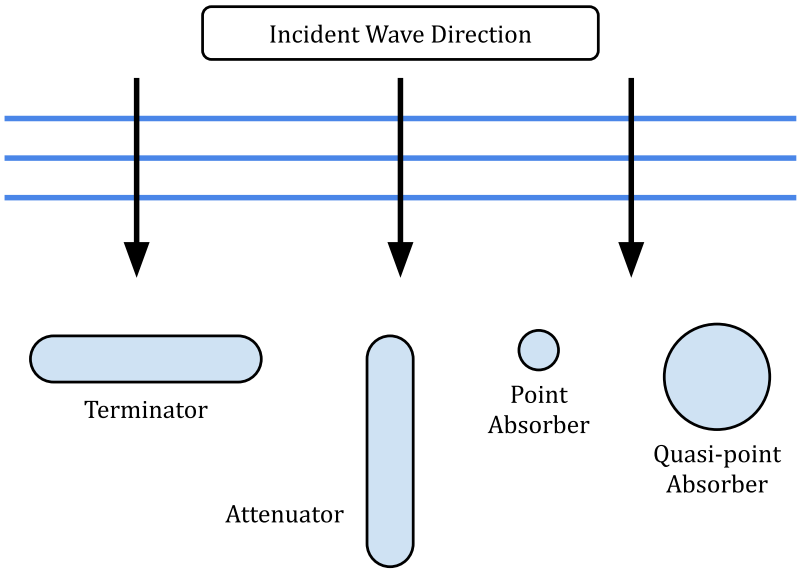

Figure 3.1: WEC classification by orientation.

Other attempts to classify WECs have led to classifications by concept [26, 34], but these approaches often lend to highly specific categories that lack flexibility for new innovations and the unique characteristics of some devices. Instead, classification by working principles has shown more versatility in classifying WECs more broadly than by concept. Additionally, these reviews also include classification by location, regarding the distance from the shoreline, with categories of onshore, nearshore, and offshore devices [35, 36, 37, 38, 32].

Classification by working principles.

Oscillating water columns (OWC) generally consist of a chamber open at the bottom that has a pocket of trapped air above the water's free surface. Passing waves generate an oscillatory motion that compresses and decompresses the trapped air driving a turbine like a fluid piston. A Wells turbine is most commonly employed as it is self-rectifying, meaning it rotates in the same direction regardless of flow direction [35].

Oscillating body systems can take many forms, but they involve transferring the kinetic energy in incident waves to wave-induced motions of floating or submerged bodies that can be converted into usable energy by the PTO [26].

Overtopping devices are constructed in a way that allows incident waves to collect water above the mean sea level and funnel through a low-head hydraulic turbine, returning collected water to the sea. The turbine converts the potential energy to electricity [36, 39].

Classification by location.

A *shoreline device* is a device that is mounted on the physical shore and may have specific requirements for their installation to fit localized shoreline geometry which may not allow for mass production [32]. These devices are not subsurface.

A *nearshore device* is a device that is in relatively shallow water which is often defined as a depth of less than one-quarter of the wavelength or moderate depths of 10-25 meters [38]. These devices are often seafloor mounted, meaning they have sufficient negative buoyancy to remain in their initial installation position, or they are physically affixed to the seafloor. These devices are often surface-piercing to some degree due to the water depth.

An *offshore device* is a device that is located in deep water which is often defined as a depth of more than 40 meters [32, 38]. These devices are moored to the seabed. These devices may be surface-piercing or subsurface.

While classification by concept is not well suited for WEC classification as a whole, subsurface WECs are a smaller subset that can be more easily categorized into six overarching archetypes. The following subsurface WEC archetypes are defined to provide structure to the proceeding sections.

Subsurface WEC archetypes.

Submerged point absorber: a device whose mooring system provides the reaction point for the PTO, small dimension in comparison to incident wavelength, axisymmetric float design, omnidirectional, designed for the nearshore or offshore [40, 41, 42, 43]

Submerged OWCs: similar to conventional OWC designs, but adapted to a submerged design, designed to be seafloor mounted in the nearshore [44]

Submerged pressure differentials: typically devices with lengths on the order of half a wavelength that leverage spatially varying pressure differentials in the wave field to drive a fluid flow, designed for the nearshore [45, 46]

Oscillating surge: a device generally consisting of one or more flaps that move back and forth on hinged joints, driven by the horizontal particle velocity of a wave which generates a surging motion, designed for the nearshore [47, 48]

Bulge wave: devices that generate bulge waves within a long flexible body to generate power, designed for the nearshore [49, 50]

Flexible membrane: a device that covers a large area and leverages spatially varying pressure differentials to absorb the energy of incident waves, designed for the nearshore [51, 52]

3.2 Subsurface WEC Development

Submerged Point Absorbers

One of the first successful submerged WEC designs was the Archimedes Wave Swing (AWS), an offshore, fully submerged device [5]. The AWS consists of an air-filled chamber with two main components, a "silo" and a "floater". The silo is open at the top and moored to the seabed, and the floater encloses the top. Under a wave crest, the floater compresses the air within the chamber and then acts like an air spring, returning the floater to the top under a wave trough. This reciprocating linear motion of the heaving floater is converted to electrical energy. A cut-away image of these mechanics is shown in Figure 3.2. A 2MW prototype was built and tested in 2004 and remains a prevailing patented technology of AWS Ocean Energy today. The AWS is still under development with future testing planned in 2023 [40].

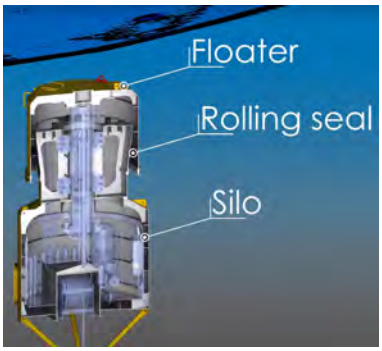

Figure 3.2: AWS Ocean Energy's AWS internal mechanics [53].

The originators of the AWS also developed the Symphony WEC which is now managed by Symphony Wave Power [41]. The Symphony WEC works similarly to the AWS. A "hull" reacts off a "core", a cylindrical pipe that is connected to the seabed. The heaving of the hull is converted to usable energy via a bidirectional turbine PTO. The liquid inside an internal membrane is pushed through the turbine and into a spring chamber. The device can be tuned to be resonant with the waves by changing the pneumatic spring in the system [41]. A cut-away image of these mechanics is shown in Figure 3.3.

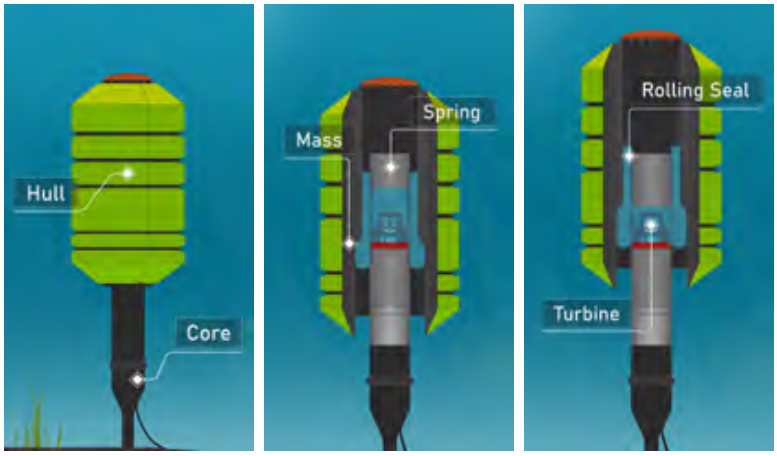

Figure 3.3: Symphony Wave Power's Symphony internal mechanics [10].

Carnegie Clean Energy first introduced its heaving buoy concept in 1999, with the first sea trials of CETO 1 in 2006 [54]. The CETO 1 was a spherical buoyant actuator but the design has evolved in shape and size with each subsequent iteration. The current generation has moved toward a slightly beveled, slim, cylinder-shaped buoyant actuator. The CETO 2 (2008), CETO 3 (2011), and CETO 4 (2012), all single-leg moorings, saw moderate success with power ratings of 1kW, 80kW, and 180kW, respectively [7]. However, a real significant impact was seen in Carnegie Clean Energy's CETO 5 (2013) and CETO 6 (2016). Illustrations of these designs are shown in Figure 3.4. The diameter of the buoyant actuator was found to have a considerable influence on the power output, and the diameter from the CETO 5 design was increased from 11 meters to 20-25 meters in the CETO 6 design. Another significant shift between CETO 5 and CETO 6 was the change to a three-tether mooring system from the longstanding single-leg mooring. The expected increase in power rating is from 240kW to 1.5MW [8]. A significant investigation has gone into this type of point absorber design, mainly from research groups in Australia, the location of Carnegie Clean Energy.

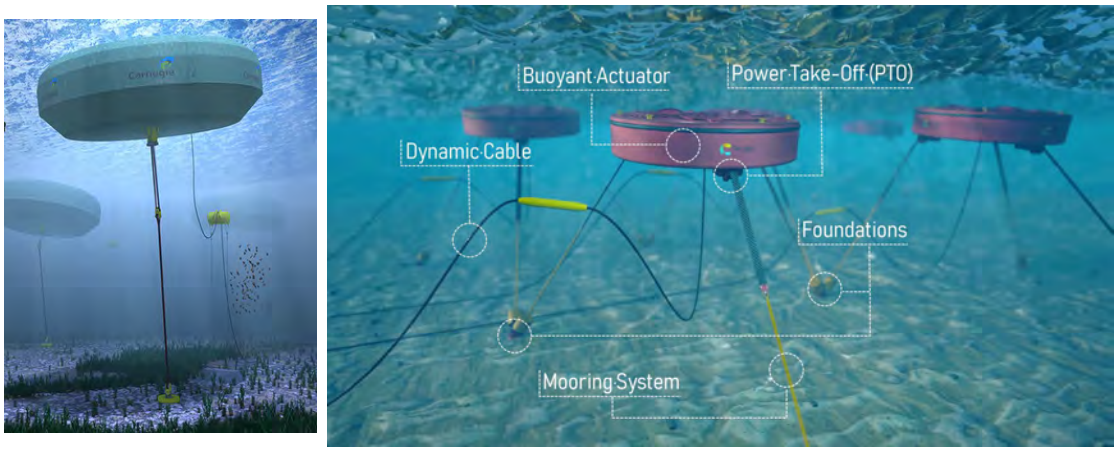

(a) CETO 5 [55].

(b) CETO 6 [56].

Figure 3.4: Carnegie Clean Energy's CETO designs.

In a more recent development, CalWave deployed its xWave pilot unit in 2021, the Company's and California's first at-sea wave energy project. The unit completed a 10-month deployment, remaining operational 99% of the time, and the collected data will be used to inform the design of the next generation of their xWave series. The prototype was a 14-foot by 14-foot chamfered box-shaped device with the ability to operate at different depths of submergence [57]. An image of the device is shown in Figure 3.5. CalWave has not provided much publicly available information on their device, nor has any research focused on a point absorber with a box-shaped float or a four-tether design. However, the company has been selected for a two-year deployment at PacWave South, an open ocean wave energy testing facility off the coast of Newport, Oregon, to validate their larger x100 device which could reach upwards of 500 MW of power [43].

Figure 3.5: CalWave's xWave pilot out of the water [43].

Submerged OWC

Traditional, surface-piercing nearshore OWCs are well-defined compared to other WEC technologies. OWCs had early commercial success in WEC technology development in 1945 with Japanese inventor, Yoshio Masuda, who invented an OWC capable of generating power for navigation buoys [58]. However, despite OWCs' longstanding place in the WEC technology space, they have not been targeted for subsurface designs. A conceptual design of a submerged variation of the oscillating water column (OWC), termed the "resonant sea wave energy converter" (REWEC), was first proposed by Boccotti in 2003 [59] and numerically analyzed in 2008 by [44]. The REWEC is a conceptual design and has not been developed further.

Submerged Pressure Differential

A highly robust submerged pressure differential WEC concept, the Delos-Reyes Morrow Pressure device (DMP), was originally conceived, studied, and tested at Oregon State University in 1991 [45]. The DMP consists of flexible air-filled chambers connected with a bi-directional air turbine, depicted in Figure 3.6a. As waves pass over the device, pressure fluctuations generate alternating compression and expansion cycles of the chambers, forcing air through the turbine which drives an electrical generator. The system is fully submerged, seafloor mounted, designed for water depths up to 30 meters, and suitable for close packing in an array. For best performance, [60] found the distance between each pair of deformable chambers to be close to half the wavelength of the spectrum peak frequency and that the device should be oriented parallel to the incident wave direction to maximize the excitation pressure. The DMP was patented in 2013 and is now managed by M3 Wave Energy Systems, LLC.

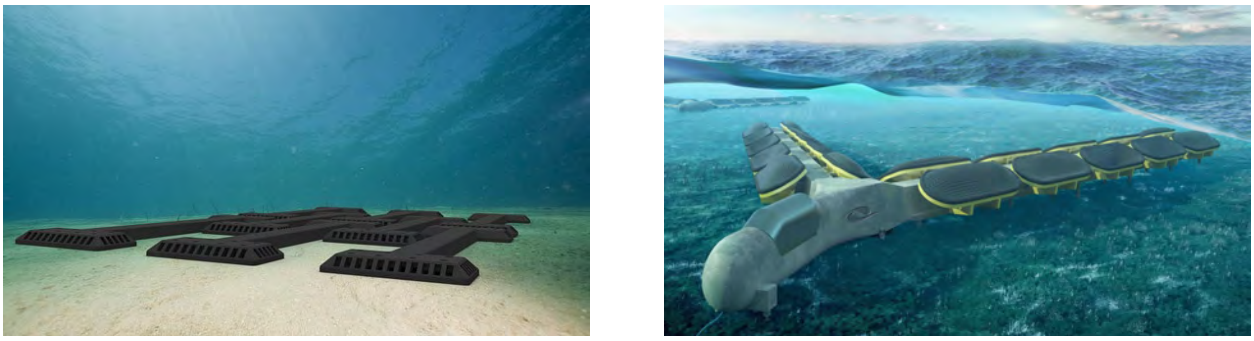

(a) M3 Wave Energy Systems, LLC's DMP [61]. (b) Bombora Wave Power's mWave [46].

Figure 3.6: Commercialized examples of submerged pressure differential WECs.

Bombora Wave Power, founded in 2011, put forth a similar concept comprised of a series of air-inflated flexible membranes mounted to a structure, shown in Figure 3.6b. The design

of the device is that it be longer than the wavelength so that there are cells consistently being simultaneously compressed and decompressed to drive a turbine [54]. The PTO consists of a unidirectional flow turbine that drives a generator. Bombora Wave Power markets their mWave device as scaleable, with different arrangements of the structure the cells are attached to, modular, in regards to their cell modules and PTO, and robust, with no external movable parts other than the flexible rubber membranes of the cells [46]. In 2018 they secured a grant to deploy a full-scale 1.5 MW mWave prototype [62]. Bombora has plans for a grid-connected mWave device and commercial projects involving wind platform integration for 2021-2025 [46].

Oscillating Surge

Significant research has gone into oscillating surge wave energy converter (OSWEC) designs. Sandia National Laboratory (SNL) and National Renewable Energy Laboratory (NREL) collaborated on a floating OSWEC (FOSWEC) design. The first prototype FOSWEC was tested in 2015 at a 1:33 scale, and the second version FOSWEC2 in 2020 in the Directional Wave Basin at Oregon State University's (OSU) Hinsdale Wave Research Laboratory (HWRL) [48, 47]. Figure 3.7 shows an image of SNL and NREL's FOSWEC2 design during experimental testing.

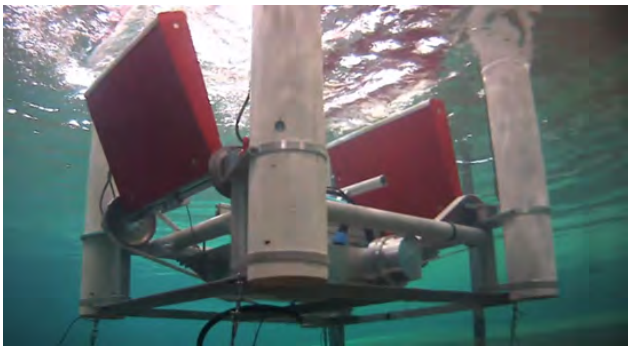

Figure 3.7: SNL & NREL's FOSWEC2 design in the OSU's directional wave basin [63].

Although designed to be semi-submerged, FOSWEC, as well as commercialized oscillating surge WECs, can be extrapolated to fully submerged designs. Commercialized designs include Langlee Wave Power's Robusto [64], Aquamarine Power's Oyster [65], AW-Energy's WaveRoller [66], BioPower System's bioWave [67], and Resolute Marine's $Wave_2O$ [68]. Many of these commercialized devices are seafloor mounted, with only Langlee's Robusto designed for a floating application. Examples of these oscillating surge devices are depicted in Figure 3.8.

(a) Langlee Wave Power's Robusto [64].

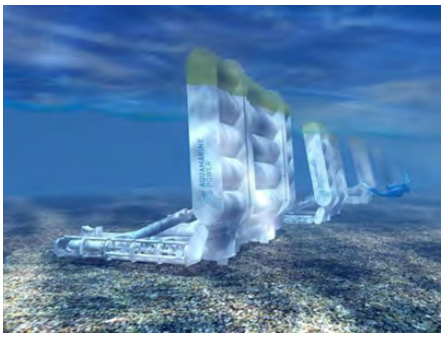

(b) Aquamarine Power's Oyster [65].

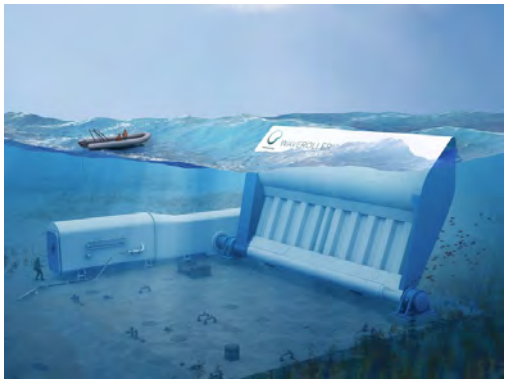

(c) AW-Energy's WaveRoller [66].

(d) BioPower Systems' bioWave [67].

Figure 3.8: Commericalized examples of oscillating surge WECs.

Bulge Wave

An entirely new concept emerged in 2006, the Anaconda, later classified as a "bulge wave" WEC, consisting of a closed rubber tube filled with slightly pressurized water anchored head into the seas. As waves pass over the device, pressure variations create bulge waves internally within the tube and drive a turbine housed in the tube's stern or distributed along the tube. The concept was inspired by the aortas of mammals in which the pressure pulses of the heart generate bulge waves. Experimental testing of a 1:25 scale model was conducted at the wave basin at Danish Hydraulic Institute [49]. A few years later, another bulge wave device, the S3 Wave Energy Converter (S3 WEC) was in development at SBM Offshore with an entirely novel PTO system. Instead of a turbine PTO, the tube itself was made of electro-active

polymer (EAP) which acted as both structural material and the PTO. The EAP generates electricity with changes in capacitance caused by radial deformations of the tube as bulge waves are generated. Experimental testing was conducted in the Hydrodynamics and Ocean Engineering Tank of Ecole Centrale de Nantes for a 10-meter scale model [50].

(a) Checkmate Seaenergy's Anaconda [69]. (b) SBM Offshore's S3 WEC [70].

Figure 3.9: Bulge Wave WEC concepts.

Flexible Membrane

In 2012, a flexible membrane design was proposed in [51] from the University of California, Berkeley. Inspired by the strong wave damping over muddy seafloors, the Wave Carpet WEC concept sought to emulate this phenomenon through a synthetic seabed carpet consisting of a carpet mass attached to linear, vertically acting PTOs. The PTOs are horizontally distributed and seafloor mounted. Experimental testing by [52] demonstrated a peak experimental PTO (hydraulic) efficiency of 42.3% and an absorption efficiency of 99.33%. However, the manufacturing of a suitable flexible material for the synthetic seabed carpet at full-scale remains a challenge for this WEC to reach commercialization.

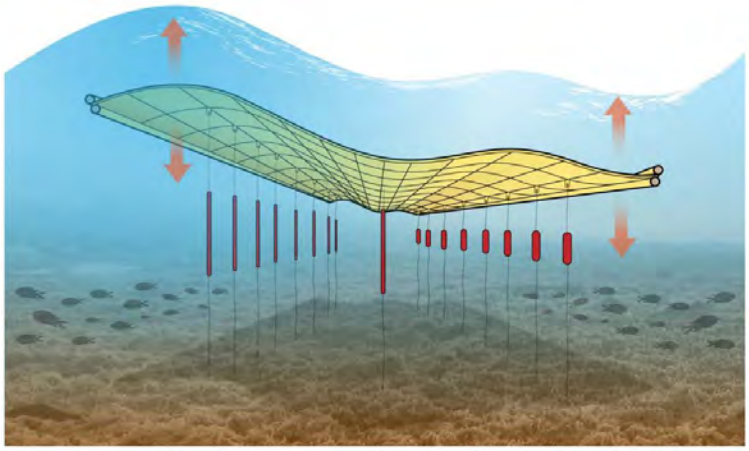

Figure 3.10: An illustration of a flexible membrane device by Al Hicks, NREL [71].

Current Status of Subsurface WECs

A summary of industry examples, commercialized or thoroughly researched prototypes, are listed in Table 3.1. Many commercialized OSWECs exist, but again, these WECs are semi-submerged and are not currently being designed for greater depths of submergence.

WEC Device	Source	Classification
AWS	AWS Ocean Energy	Point Absorber [40]
Symphony	Symphony Wave Power	Point Absorber [41]
CETO	Carnegie Clean Energy	Point Absorber [42]
xWave	CalWave	Point Absorber [43]
DMP	M3 Wave Energy Systems, LLC	Pressure Differential [45]
mWave	Bombora Wave Power	Pressure Differential [46]
FOSWEC	SNL & NREL	Oscillating Surge [48]
Robusto	Langlee Wave Power	Oscillating Surge [64]
Oyster	Aquamarine Power	Oscillating Surge [65]
WaveRoller	AW-Energy	Oscillating Surge [66]
bioWAVE	BioPower Systems	Oscillating Surge [67]
$Wave_2O$	Resolute Marine	Oscillating Surge [68]
Anaconda	Checkmate Seaenergy Ltd	Bulge Wave [49]
S3 WEC	SBM Offshore	Bulge Wave [50]
Wave Carpet	UC Berkeley, USA	Flexible Membrane [51]

Table 3.1: Industry examples of submerged WECs.

Bulge wave and flexible membrane devices pose challenges in their construction with the need for special materials. Pressure differential devices show promising performance, but realistically need to be seafloor mounted to allow adequate compression of their membranes which limits the water depths they can be deployed in. Oscillating surge devices are really only suited for the nearshore in shallow water conditions where wave orbitals are elliptically dominant in surge for these devices to produce power [32]. Of all the WEC devices, point absorbers are the best adapted for offshore applications for they are well suited for deep water conditions where wave orbitals are circular as these devices typically produce power in heave with potential contributions in surge and pitch [72]. They also have the advantage of mooring systems being more easily adaptable to different water depths while keeping the depth of submergence of the float the same. Point absorbers can also be more readily manufactured with materials and methods typical of their surface-piercing counterparts with component strengths capable of withstanding the extreme wave conditions present offshore. In consideration of these advantages, this literature review proceeds with a focus on submerged point absorbers.

3.3 Submerged Point Absorber Research

The bulk of literature regarding submerged point absorbers focuses on a sphere or a cylindrical shape float influenced by Carnegie Clean Energy's CETO designs. The two most prominent CETO designs research is based on is the CETO 5 and CETO 6, which are single-tether and three-tether systems, respectively.

In 2015, researchers at Carnegie Clean Energy (then called Carnegie Wave Energy Ltd.) analyzed wave loading on a CETO 5 1:20 scale model in extreme sea states [73]. They used linear and nonlinear numerical methods and compared them to wave tank experimental data. Through numerical simulations in OpenFOAM, an open-source computational fluid dynamics (CFD) software, they obtained estimated drag coefficients. The float modeled was a beveled cylinder with outer dimensions of 20 meters in diameter and 6 meters in height. Experimental testing concluded that under moderate wave conditions, the linear time domain solver overestimated load and motion predictions, and the fully nonlinear solver provided better results.

In 2016, Sergiienko et al. investigated the optimal tether inclination angle for maximum power absorption in a three-tether mooring design [74]. They conducted two studies, a purely kinematic analysis with no specification of buoy shape and a dynamic analysis of spherical and cylindrical buoys with different aspect ratios. They found the optimal tether inclination angle to decrease with flatter cylinders (smaller aspect ratios of buoy height to radius). This tracks with theory: the optimal inclination angle for a vertical heaving device is 0° and 90° for a fully surging device. Thus, it is expected that as the height of the cylinder increases, the excitation force in surge increases, and the optimal tether angle should increase with it.

Later in 2016, the same group also analyzed a sphere and four cylinders with different aspect ratios to understand the effect of the buoy geometry in a three-tether design [72]. They compared 1-tether and 3-tether configurations in irregular waves with a range of tether angles (30-60° in 1° increments). Their analysis found that for a cylinder with an aspect ratio of h = 0.5a, the optimal tether angle is $\alpha = 30°$. They also concluded that from a PTO design point, the flattest cylinder (H = 0.5a) of those studied was the best choice. In addition, they found that a 3-tether WEC can theoretically absorb 1.6 - 2.3 times more power than a 1-tether WEC using the same buoy.

To thoroughly understand the distinctions between floating and submerged point absorbers Sergiienko et al. also conducted a study of spherical and cylindrical shaped buoys in regular and irregular waves using a linear wave theory and assuming an infinite water depth [75]. They found that the bandwidth decreases as the submergence depth of the buoy increases, but for a narrow range of wave periods, the performance of a submerged cylindrical buoy could be superior to that of a floating one. Based on power absorption limits in regular waves, a cylinder with a height of 5.5 meters and diameter of 11 meters, submerged at 3.75

meters, could potentially absorb more power than a floating counterpart at wave periods between 7 and 10 seconds. They also concluded that submerged cylindrical buoys should be 1.4-2.2 times larger than a floating counterpart to generate the same amount of power when submerged at a depth of 1.2 times the radius.

In 2018, Sergiienko et al. took the previous work further and accessed the estimation of energy delivery and techno-economic metrics of a submerged point absorber similar to the CETO three-tether system [76]. They found that for a three-tether system, when one tether is aligned with the direction of wave propagation, the PTO inline with that tether generates approximately 45% of the total mean power and the other two PTOs account for the rest of the energy in equal share, which was also shown in their 2016 study with a float with a different aspect ratio. For their selected buoy geometry and tether inclination angles they saw 50-55% of the energy being generated from heave and 45-50% produced by surge. This is in contrast to a single-tether design which generates 90-95% of its energy from heave and only about 5% of its energy from surge, with pitch having a negative effect on power production. They also analyzed system sensitivity to buoy mass, tether stroke, and tether angle. Their results showed that a lighter buoy can generate more energy, but at the cost of increased loading on the mooring system by 1.4 times. The length of the tether stroke was found to only marginal increases in average power of only about 2% if the control parameters have been optimized. The tether inclination angle and tether attachment point angle were also found to be fairly insensitive, with only a 5% reduction in power with $\pm$ 5° from its optimal value. Overall, they concluded that the three-tether WEC can produce cheaper energy as compared with a single-tether configuration.

Building upon the findings of previous work, several optimization studies have furthered this work on submerged cylindrical-shaped multi-tether point absorbers. In 2020, Sergiienko et al. looked at two objective functions, maximizing annual average power output and minimizing the levelized cost of energy (LCoE), however, these are contrasting aims and produce vastly different results [77]. In maximizing power, the result was a cylinder of 40 meters in diameter and the largest possible height (30 meters). In minimizing LCoE, a cylinder of 11-14 meters in diameter with the smallest possible height (aspect ratio of 0.4). The results coincided with Carnegie Clean Energy's CETO 6 design. Later that same year, Neshat et al. conducted a similar study with the same two objective functions using a bi-level optimization framework, and their results found good agreement with Sergiienko et al's earlier study [78].

In 2022, Tran et al. also investigated a CETO 6 design, specifically regarding the behavior of each hydrodynamic mode and coupling effects [79]. Results showed that for regular waves the tether configuration should be set to leverage surge and heave modes to maximize power absorption. However, in irregular waves, they found that the optimal design became largely dominated by surge. They concluded that for overall maximum power, all three tethers

should be attached close to one another at the bottom of the float.

Gaps in Research

Of the current published literature, there lacks research focused on a singular cohesive study that investigates increasing the number of tethers from a single to three-tether and extending it to four and five-tether configurations for a submerged point absorber with a coupled PTO-mooring system. Industry examples include submerged point absorber WECs in the late stages of development which show varied design choices in this characteristic. AWS Ocean Energy's AWS, Symphony Wave Power's Symphony, Carnegie Clean Energy's CETO, and CalWave's xWave, have chosen single-tether, three-tether, and four-tether mooring configurations and lack consensus on a seemingly fundamental aspect of WEC hydrodynamic and power performance. Research has largely been concentrated on the CETO device, with little to no literature regarding the single-leg moored AWS design (other research has been done on a seafloor-mounted version) or the Symphony device. Nor is there published research focused on a box-shaped float or four-tether design similar to the xWave. Of the literature regarding CETO's design, investigations have been primarily focused on comparing their single-tether and three-tether configuration, and on the optimization of parameters for the CETO 6 design.

This thesis seeks to explore the effect of the mooring configuration and the corresponding number of PTOs on a submerged point absorber WEC. The following study uses a float with simple geometry to best isolate this aspect in the analysis of each configuration's performance. This work constitutes a full comparison of single, three, four, and five-tether configurations with uniform parameters to allow for practical comparison, which is not currently found in the literature.

Chapter 4

Methodology

The following sections provide the methods used in the hydrodynamic modeling and numerical analysis of this study. Section 4.1 presents the ProteusDS modeling approach for a submerged WEC, including a detailed description of the PTO implementation. Section 4.2 describes the process to identify WEC response amplitude operators (RAOs) and how PTO damping values were selected. Section 4.3 lays out the procedures followed for the irregular wave and energy decay simulations as well as how performance metrics were calculated.

4.1 ProteusDS Modeling

The WEC hydrodynamic body and mooring system is implemented using standard practices found in the ProteusDS manual [15] and tutorials [29]. The hydrodynamic body is created as a rigid body DObject and utilizes ProteusDS' rigid body feature option to mesh basic geometric shapes. For a submerged one-body WEC, the mooring system acts as a reaction point and is under constant tension. The requirements of such a mooring system include minimal stretching and the ability to withstand persistent and large tension forces. To meet these demands, Dyneema from the ProteusDS Parts Library [80] is chosen as the material to model individual tethers for its high strength, low stretch, and wear resistance characteristics [81] with ProteusDS' dynamic cable DObjects. ProteusDS does not provide a direct way to add a PTO into a model, instead, they recommend using an ABA connection joint to emulate PTO dynamics. This procedure is not detailed in any ProteusDS documentation. The implementation of a linear direct drive generator PTO is now presented. A simplified diagram of a linear direct drive generator PTO is used as a framework, shown in Figure 4.1.

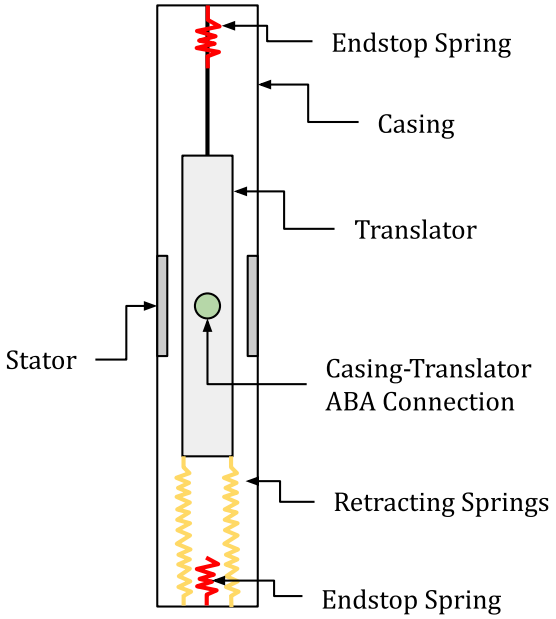

Figure 4.1: Simplified linear PTO diagram.

Following this diagram, a rigid body casing and translator are created and given rigid body cylinder features. A rigid body ABA connection joint is made between them and the joint type is set to prismatic which is a single DoF joint that constrains motion between two rigid bodies to translation along a common axis. The casing is made the master and the translator is made the follower. The follower joint axis is set to the z-axis to constrain translation only in z so that the translator may only oscillate up and down in line with the casing. The connection is given a rigid body ABA connection joint feature, referred to as the PTO joint, that defines end stops, joint stiffness (K_{PTO}), and joint damping (C_{PTO}). The end stop springs are implemented by setting the location of the end stops with respect to the desired translator stroke range and an end stop stiffness to a value that will ensure translator oscillations are restricted to the physical length of the casing.

For submerged WECs, a restoring force is an essential component of the system design. Unlike their surface-piercing counterparts, subsurface WECs do not have a restoring force provided by gravity. Instead, a restoring force must be included to ensure the translator is not forced to the top of its stroke and halted in its oscillation. This restoring force is provided by the retracting springs. In [76, 79], this restoring force is included in the PTO force equation as a constant force value, however, ProteusDS does not allow this. Instead, the restoring force is implemented in the PTO joint stiffness, and the restoring force is dependent on the relative displacement between the translator and casing. For a linear PTO, the PTO force (in Newtons) is calculated with Equation 4.1.

$$F_{PTO} = -K_{PTO}X_{rel} - C_{PTO}\dot{X}_{rel} \tag{4.1}$$

where X_{rel} is the displacement between casing and translator and $\dot{X}_{rel}$ is the relative velocity between the casing and the translator. The restoring force provided by F_{PTO} must balance the buoyancy force in an equilibrium position. In an equilibrium position the relative velocity between the casing and the translator is zero and only the $K_{PTO}X_{rel}$ term remains to provide the force to balance the force of buoyancy, F_b (in Newtons), which is calculated with Equation 4.2.

$$F_b = (m_w - m_b)g \tag{4.2}$$

where m_w is the mass of the displaced water, and m_b is the mass of the hydrodynamic body. The mass of displaced water is simply $m_w = \rho V$ where V is the displaced volume of the WEC hydrodynamic body. Regardless of the number of PTOs in the system (N), all PTOs are set to the same joint stiffness value and assumed to share an equal contribution to the restoring force. The value of K_{PTO} to balance F_b is calculated with Equation 4.3.

$$K_{PTO} = \frac{F_b}{N \cos \alpha} \tag{4.3}$$

where α is the angle of the tether connected to the PTO measured from the z-axis. The cosine of α isolates the vertical component. Due to dependence on displacement, the translator does not reach an equilibrium position until it travels one meter from its initial joint position in a no wave condition. For the translator to reach an equilibrium state at the center of the casing, the joint between them is made at the center of the translator and one meter down from the center of the casing.

4.2 Preliminary Simulations

Before running any specific wave conditions, RAOs are created for the system. Following the identification of peak responses in the RAOs, an exhaustive damping search can be carried out to find "optimal" damping values for the PTO. Once these values are found simulations of regular and irregular wave conditions for analysis can be run. Regular wave simulations are run in ProteusDS and utilize an Airy wave model. Winds and currents are not included. Regular wave simulations are run for 300 seconds (5 minutes) and the wave ramp up time is set to 60 seconds. Wave heading (θ), wave height (H), and wave period (T) are set in the Environment input file [28].

RAOs

RAOs describe a rigid body's motion amplitude ratio to a wave amplitude at a specified wave period and DoF [29]. To identify a rigid body's RAOs, regular waves with a unit wave height of one meter are run across wave periods without PTO damping. For each rigid body and DoF, the response amplitude is calculated at each wave period interval. The response amplitude is then normalized by the wave height, which then fully describes the RAO for the rigid body in the specified DoF. RAOs, specifically displacement RAOs for the WEC rigid body and PTO translator stroke are used to determine resonant periods for the system. RAOs for WEC rigid body surge, heave, and pitch are calculated by finding the range of its displacement from the ProteusDS position data output. Similarly, the PTO translator stroke is calculated from its range of displacement in heave (for a linear direct drive PTO). RAOs are calculated with a wave period resolution of 1 second, and any apparent peaks in the RAO responses are swept again with a wave period resolution of 0.5 seconds.

Exhaustive PTO Damping Search

An exhaustive damping search is a simpler alternative to running a full damping optimization which is more computationally expensive. An exhaustive damping search is the method chosen to reduce the number of simulations needed to identify an "optimal" PTO damping value, and is based on maximum instantaneous power. The exhaustive damping search is run with regular waves while choosing different PTO damping values. Waves are run with a unit wave height of one meter and at the wave period of the translator stroke's peak response identified from RAOs. The PTO damping value is then swept through an initial range of selected values, and additional sweeps are conducted around any apparent peaks in maximum instantaneous power. Once a clear peak in maximum instantaneous power is found, the PTO damping value at that location is deemed the optimal PTO damping value. This identified value is then used for all subsequent wave simulations.

For a linear direct drive generator PTO, the instantaneous power time series, P_{PTO}, is calculated from the PTO damping and time series of the relative velocity between the PTO translator and casing using Equation 4.4 [79]. To clarify, this is mechanical power, not electrical power, and power is in terms of the rate of work done by the relative velocity between the casing and the translator.

$$P_{pto} = C_{pto}\dot{X}_{rel}^2 \tag{4.4}$$

Maximum instantaneous power (in watts) is taken as the maximum value in the instantaneous power time series sufficiently outside the wave ramp up time to ensure the value selected is not part of the initial stabilization of the dynamics.

4.3 Wave Simulations

Before running irregular waves, additional regular wave simulations are run at wave conditions of interest and include the optimal PTO damping value found in the exhaustive search. While regular waves are not representative of real sea states, these simulations can provide insight into the basic system responses, and assist in interpreting the results of irregular wave simulations. Irregular wave simulations are run in ProteusDS and utilize a PM or JONSWAP wave model. Winds and currents are not included. Irregular wave simulations are run for 1200 seconds (20 minutes) and the wave ramp up time is set to 60 seconds. Wave heading (θ), significant wave height (H_s), spectrum peak period (T_p), the peak shape constant (γ), the wave seed, the number of wave segments, and the wave spreading function (optional) are set in the Environment input file. The wave seed sets the random number generator seed value for the wave spectrum and influences properties such as the initial wave phase and heading for spectral sea state wave components [15]. The number of wave segments sets the number of discrete wave segments used to reconstruct the desired wave spectrum. Use of the wave spreading function (cosine exponential) results in short-crested waves, while no spreading results in long-crested waves [28].

To ensure there are enough wave segments to prevent a repeating sea surface, Proteus recommends the following calculation shown in Equation 4.5 [15].

$$WaveSegments_{min} = \frac{SimulationTime}{2\pi(\omega_{max} - \omega_{min})} \tag{4.5}$$

where $\omega_{min} = 0.25{*}\omega_p$ and $\omega_{max} = 4{*}\omega_p$. The peak wave frequency ω_p is simply calculated from the peak wave period with $\omega_p = 2\pi/T_p$. The number of wave segments used for each simulation is calculated using the specified wave climate's peak wave period (rounded up to the nearest whole number).

Energy Generation

The energy generation (in watt-hours) is calculated by summing the integrated instantaneous power time series from t_1 to t_2 from each PTO and dividing it by the fraction of an hour covered by the duration of the series integrated, as shown in Equation 4.6 [82]. This ensures appropriate scaling of the energy generation to the unit of watt-hours.

$$E_{gen} = \frac{(t_2 - t_1)}{3600}\left[\sum_{i=1}^{\#ofPTOs}\int_{t_1}^{t_2} P_{pto,i}\,dt\right] \tag{4.6}$$

For regular waves, integration is done over the last 60 seconds of the simulation when the simulation has reached a steady-state response. For irregular waves, integration is done from 120 seconds (twice the ramp up time), deemed sufficiently outside the initial stabilization of

the dynamics, until the end of the simulation.

Coefficient of Variation

The coefficient of variation (COV) describes the temporal variability of power generated by the WEC. It is calculated by dividing the standard deviation of the instantaneous power time series by the mean instantaneous power (denoted by the over bar). The COV is used as a metric for power quality and is a nondimensional value. A higher value of COV indicates a less steady power source [83].

$$COV = \frac{\sqrt{(P_{WEC} - \overline{P_{WEC}})^2}}{\overline{P_{WEC}}} \tag{4.7}$$

Capture Width

The capture width (CW) of a WEC is the ratio of the average absorbed wave power, P_{WEC} (in watts), to the average incident wave power J (in watts per meter), as shown in Equation 4.8 [26]. CW has units of meters.

$$CW = \frac{P_{WEC}}{J} \tag{4.8}$$

Capture Width Ratio

The capture width ratio (CWR) or η_1, is a hydrodynamic efficiency metric and is calculated by dividing the CW by the characteristic dimension, B (in meters), of the WEC, as shown in Equation 4.9 [84]. This is a nondimensional value and represents the fraction of the wave resource absorbed by the WEC. A WEC can have a CWR of greater than 1, implying it absorbs more power than is contained in a wave of its width [26]. This may happen if the WEC is designed or controlled to resonate and move with larger amplitudes than the waves themselves [85].

$$\eta_1 = \frac{CW}{B} \tag{4.9}$$

Chapter 5

Case Study

The WEC used in this study is a submerged one-body point absorber, consisting of a single cylindrical float and a coupled PTO-mooring system. The PTO is a direct drive linear generator, with an anchor that allows the PTO assembly to freely rotate to align with the tending of the mooring line. The standard WEC parameters used in this study are outlined in Table 5.1. Appendix 8 contains ProteusDS input files that list all parameters in full.

Parameter	Symbol	Value
Float height	H	$5\,\mathrm{m}$
Float radius	a	$12.5\,\mathrm{m}$
Float mass	m	$1.99 \times 10^6\,\mathrm{kg}$
Moments of inertia	$I_{xx} = I_{yy}$	$8.18 \times 10^7\,\mathrm{kg\,m^2}$
	I_{zz}	$1.55 \times 10^8\,\mathrm{kg\,m^2}$
Linear damping values	$B_{v,1} = B_{v,2}$	$2.8 \times 10^5\,\mathrm{N\,s/m}$
	$B_{v,3}$	$1.9 \times 10^5\,\mathrm{N\,s/m}$
	$B_{v,4} = B_{v,5}$	$2 \times 10^7\,\mathrm{N\,s/m}$
PTO casing length	l_{casing}	$6\,\mathrm{m}$
PTO translator length	$l_{translator}$	$3\,\mathrm{m}$
Endstop stiffness	$KEJoint$	$1 \times 10^8\,\mathrm{N/m}$
Submergence depth	d_s	$6.5\,\mathrm{m}$
Water depth	h	$100\,\mathrm{m}$

Table 5.1: Standard WEC model parameters.

The float radius, height, mass, and submergence depth are based on a study of design considerations for a three-tether WEC influenced by Carnegie Clean Energy's CETO 6 design [79], and values for the moments of inertia, and linear damping values are taken from [86] who studied a float with the same geometry to analyze PTO model predictive control. The endstop stiffness value is taken from [72] in which they used a uniform value for various spherical and cylindrical-shaped WECs.

5.1 Configurations

This case study analyzes four coupled PTO-mooring configurations: single-tether, three-tether, four-tether, and five-tether configurations. Each configuration is defined by the following set of parameters:

- **Tether Spread** ($\boldsymbol{\alpha}$): the angular spacing of tethers (in plan view) and is assumed to be evenly distributed for the number of tethers used in the configuration
- **Tether Attachment Point** ($\boldsymbol{x_{TA}}$): the horizontal distance from the center of the float where the tether connects with the float (on the bottom plane of the float)
- **Tether Inclination Angle** ($\boldsymbol{\alpha_t}$): the angle of the tether from its attachment point down to its connection with the PTO assembly, specifically the translator, measured from the z-axis
- **Wave Heading** ($\boldsymbol{\theta}$): the wave heading used to distribute loading on the tethers with regard to the configuration geometry

A diagram specifying the location of parameters is illustrated in Figure 5.1, using the three-tether configuration as an example. All other configurations follow the same approach but are not individually shown. These parameters are unique to each configuration and are listed in Table 5.2.

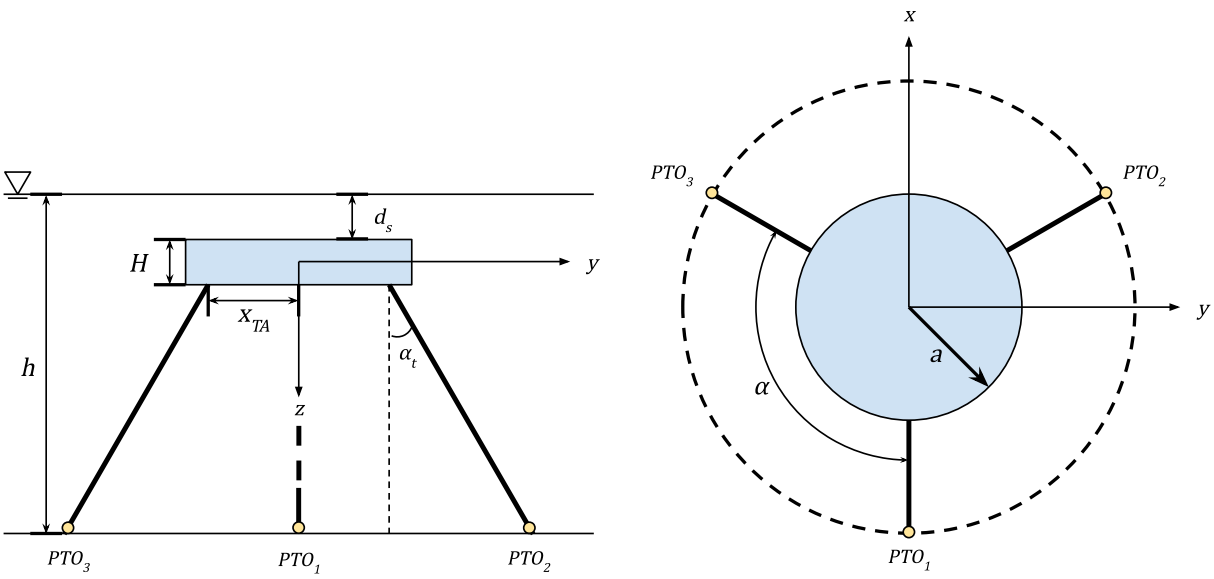

Figure 5.1: Diagram of parameter locations in side view (left) and plan view (right).

For this study, values for the tether attachment point and inclination angle are chosen from ranges found in [79, 77] but are not optimized for each configuration. These values are kept uniform for all multi-tether configurations in order to reasonably compare their results.

Configuration	Tether Spread (α)	Attachment Point (x_{TA})	Inclination Angle (α_t)	Wave Heading (θ)
Single-tether	0°	0 m	0°	0°
Three-tether	120°	10 m	30°	0°
Four-tether	90°	10 m	30°	45°
Five-tether	72°	10 m	30°	36°

Table 5.2: Configuration specific parameters.

5.2 ProteusDS Model

The WEC float is modeled with a rigid body DObject and uses the rigid body cylinder feature. Options in ProteusDS for wind loading and soil loading are turned off as the float is fully submerged at all times and does not make contact with the seabed. The buoyancy and Froude-Krylov loads are computed using the constant fully submerged buoyancy option, and hydro loading is enabled. The selected tether material is 120mm Amsteel-Blue Dyneema with properties imported from the ProteusDS Parts Library [80], listed in Table 5.3.

Parameter	Symbol	Value
Normal drag coefficient	CDc	1.5
Tangential drag coefficient	Cdt	0.045
Added mass coefficient	CAc	1.0
Axial rigidity	EA	3.37×10^8 N
Flexural rigidity	EI	302 945.063 N m^2
Torsional rigidity	GJ	302 945.063 N m^2
Diameter	D_{tether}	1.20×10^{-1} m
Density	ρ_{tether}	801.1 kg/m^3
Max breaking strength	MBS	10 771 380 N

Table 5.3: 120mm Amsteel-Blue Dyneema rope properties.

The PTO is modeled as a linear direct drive generator with the process outlined in the Methodology. An additional "anchor" rigid body DObject is created to allow the casing to align with the tending of the mooring line. A rigid body ABA connection joint is made between the anchor and the bottom of the PTO casing. The joint type is set to spherical which is a three DoF joint that allows rotation about x, y, and z, but no translation. The anchor is made the master and the casing is made the follower. The connection is given a rigid body ABA connect joint feature, referred to as the anchor joint, but no joint stiffness or damping is set, meaning the casing can rotate freely. Wind loading, hydro loading, buoyancy and Froude-Krylov loads, and soil loading are turned off for casings, translators, and anchors. The kinematics for all anchor rigid bodies is enabled, but no input is given to fix each anchor at its initial position on the seafloor. A diagram illustrating the modeled system, using the single-tether configuration as an example, is shown in Figure 5.2.

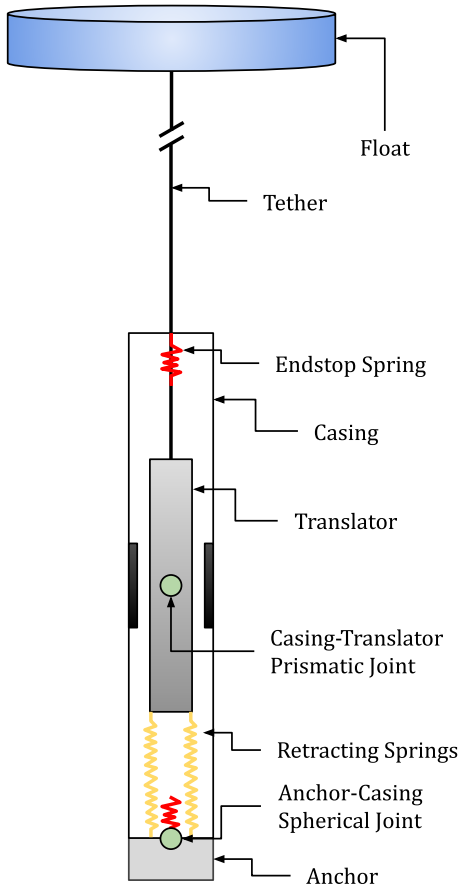

Figure 5.2: Modeled single-tether PTO system.

The force of buoyancy of the WEC float is calculated with Equation 4.2, and estimated at 5.16 MN. In initial tests to check model stability and dynamics, it was found that using the calculated PTO stiffness values from Equation 4.3 over-constrained the system and the translator was unable to reach desired stroke ranges. Therefore, the stiffness values were reduced and recalculated with $K_{PTO} = F_b/N$ instead. The PTO stiffness set for each configuration calculated with this alternative method is listed in Table 5.4. These are consistent values used in all preliminary and wave simulations for their respective configurations.

Configuration	**PTO Stiffness (K_{pto})**
Single-tether	5.16×10^6 N/m
Three-tether	1.71×10^6 N/m
Four-tether	1.29×10^6 N/m
Five-tether	1.03×10^6 N/m

Table 5.4: Calculated PTO stiffness values.

Library & DObjects Input Files

The features defined in the Library for each simulation are listed in Table 5.5. Regardless of configuration and the number of tethers and PTO assemblies, only one instance of each feature is defined but is called by multiple DObjects in the case of multi-tether configurations.

Name	Type
Float	Rigid Body Cylinder
Float Drag	Linear Quadratic Drag
Casing	Rigid Body Cylinder
Translator	Rigid Body Cylinder
Anchor	Rigid Body Cylinder
Tether	Dynamic Cable
PTO Joint	ABA Connection Joint
Anchor Joint	ABA Connection Joint

Table 5.5: Features defined in each simulation.

The general list of connections between DObjects for each simulation are listed in Table 5.6. Note, for multi-tether configurations additional sets of connections are created for each added tether.

Master	Follower	Connection Type
Float	Tether (node 0)	Point
Translator	Tether (node N)	Point
Casing	Translator	ABA (Prismatic Joint)
Anchor	Casing	ABA (Spherical Joint)

Table 5.6: General connections defined in each simulation.

The connection location between each tether node 0 and the float changes for each configuration and is calculated using the MATLAB ProteusDS Geometry Script contained in Appendix 8. For each multi-tether configuration, the ABA connection between the anchor and the casing is modified in roll and pitch to align the casing with the 30° inclination of the tether it is connected in line with. All other connection locations are the same for each configuration and are listed in full in Appendix 8.

The float and the corresponding number of tethers, translators, casings, and anchors for the configuration are generated in the DObject section. Regardless of configuration, each DObject's input parameter file containing the properties of the DObject does not change. Each DObject's data file containing the initial condition of the DObject is dependent on configuration and these inputs are calculated using the MATLAB ProteusDS Geometry Script contained in Appendix 8.

Environment & Simulation Input Files

The parameters set in the Environment and Simulation input files are listed in Table 5.7 and are used for all configurations in regular waves.

Parameter	Value	Units
Environment		
Environment Transition		
EnvironmentTransitionMode	1	Individual ramp durations and start times
WaveTransitionMode	1	Ramp duration and start time
WaveStartTime	0	s
WaveRampDuration	60	s
Mean Water Level		
MeanWaterLevelTransitionMode	0	Fixed mean water level
Seabed		
WaterDepth	100	m
CustomBathymetry	0	Disabled (Flat seabed)
Water		
WaterDensity	1025	kg/m^3
WaterKinematicViscosity	1.8E-06	m^2/s
Wave		
WaveType	1	Airy
WaveHeading	θ	degrees
WaveHeight	H	m
WavePeriod	T	s
Simulation		
Instrumentation		
IntervalOutput	0.1	s
Integration		
StartTime	0	s
EndTime	300	s
Integrator	integrator	Library input file

Table 5.7: Environment and Simulation input file parameters (for all regular wave simulations).

Modified parameters for the wave input and simulation time for irregular waves are listed in Table 5.8. Only the wave parameters and simulation end time are modified, all other Environment and Simulation parameters remain the same as those used for regular wave simulations.

Parameter	Value	Units
Environment		
Wave		
WaveType	8	JONSWAP
PeakShapeConstant	1 or 3.3	1 = PM, 3.3 = JONSWAP
WaveHeading	θ	degrees
WaveHeight	H_s	m
WavePeriod	T_p	s
WaveSeed	12345	
WaveSegments	#	
WaveSpreadingFunction	0	No Spreading
Simulation		
Integration		
EndTime	1200	s

Table 5.8: Modifications to the Environment and Simulation input parameters for irregular wave simulations.

Both PM and JONSWAP spectrums are used, but in ProteusDS, the wave type must be set to JONSWAP, and the peak shape constant controls which spectrum is constructed. The same wave seed is used for all simulations to ensure consistent simulations for all configurations. The number of wave segments is set to the calculated minimum value with Equation 4.5.

5.3 Waves Simulations

The regular wave conditions are chosen based on wave periods of interest identified from the RAO simulations with a uniform wave height of 1.5 meters for the most direct comparison. The regular wave conditions for comparison between configurations are listed in Table 5.9.

Case	Wave Height (H)	Wave Period (T)	Condition
1	1.5 m	5.5 s	Deep
2	1.5 m	6.0 s	Deep
3	1.5 m	7.5 s	Deep
4	1.5 m	8.0 s	Deep
5	1.5 m	8.5 s	Deep

Table 5.9: Regular wave conditions.

The irregular wave conditions are chosen based on the most frequently occurring conditions at PacWave South in Oregon (PWS), Wave Energy Test Site (WETS) in Hawaii (WETS), and Miami, Florida (MIA) based on wave resource assessments following International Electrotechnical Commission (IEC) standards from [87] using 2000-2010 hindcast

data. The irregular wave conditions for comparison between configurations are listed in Table 5.10.

Location	Spectrum	Peak Shape Constant (γ)	Significant Wave Height (H_s)	Energy Period (T_e)	Peak Period (T_p)
PWS	PM	1.0	1.5 m	8.5 s	9.88 s
WETS	PM	1.0	1.5 m	6.5 s	7.56 s
MIA	JONSWAP	3.3	0.75 m	4.5 s	5.00 s

Table 5.10: Irregular Wave conditions.

Simulations to analyze wave energy decay with increasing depth of submergence of the WEC's hydrodynamic body are run with regular waves. The float is submerged in 5-meter increments from a depth of submergence of 6.5 meters (baseline) down to 36.5 meters (a total of 30 meters from the baseline). The float's initial position is modified to the desired depth of submergence and the locations of tethers and other WEC components are recalculated to keep the same geometry (i.e. tethers are shortened and PTOs and anchors are moved to new positions to keep the same geometrical angles of configuration design). This process is visualized in Figure 5.3. All simulations are run with regular waves with a wave height of 2 meters and a wave period of 7.5 seconds.

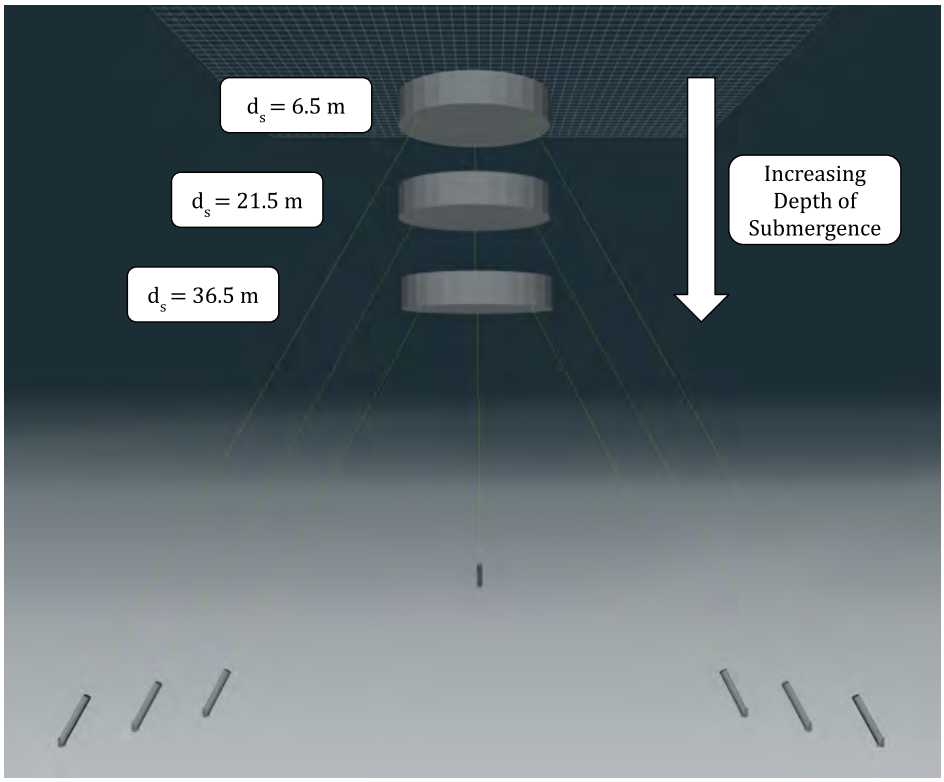

Figure 5.3: Wave energy decay model setup for example depths of submergence of 6.5, 21.5, and 36.5 meters of the float.

Chapter 6

Results

The following sections present the results of this study, which follows the same structure as the Methodology. Section 6.1 shows visuals of the case study WEC configurations modeled in ProteusDS. Section 6.2 shows the RAOs of the four configurations and the exhaustive damping search. Section 6.3 presents the results of the additional regular wave simulations, irregular wave simulations, and wave energy decay analysis.

6.1 ProteusDS Modeling

The modeled PTO in ProteusDS is shown in an enlarged view in Figure 6.1. The fully constructed models in ProteusDS for each configuration are depicted in Figures 6.2a, 6.2c, 6.2b, and 6.2d.

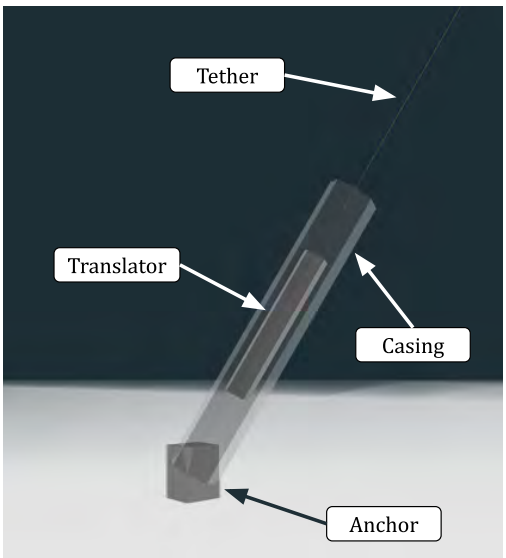

Figure 6.1: PTO showing the casing, translator, and anchor as modeled in ProteusDS.

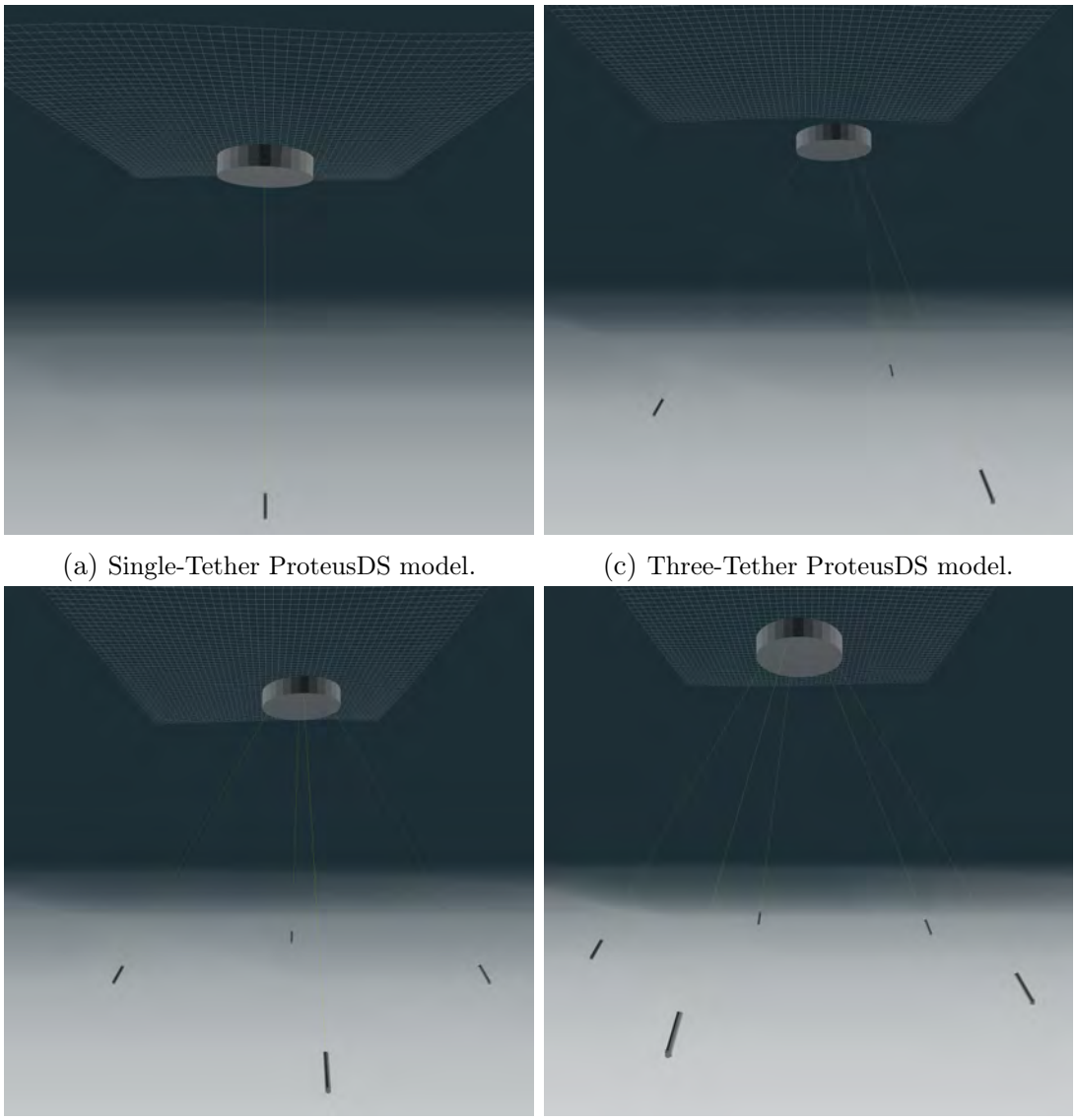

(a) Single-Tether ProteusDS model.

(c) Three-Tether ProteusDS model.

(b) Four-Tether ProteusDS model.

(d) Five-Tether ProteusDS model.

Figure 6.2: The four configurations modeled in ProteusDS.

6.2 Preliminary Simulations

RAOs

The RAOs for translator stroke, float surge, heave, and pitch are shown in Figures 6.3 6.4, 6.5, and 6.6. All response amplitudes have been normalized by the one-meter wave height input. Dotted vertical lines indicate the wave period for the primary peak translator response and any secondary peaks of the specified configuration. Plots are shown with continuous lines to help identify trends, but symbols indicate actual data points from simulations.

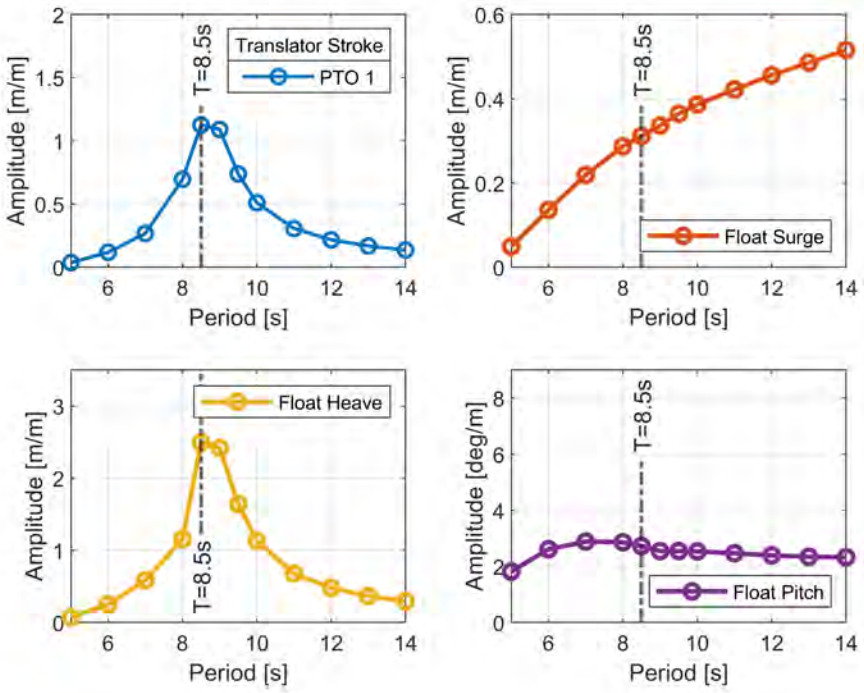

Figure 6.3: Single-Tether RAOs.

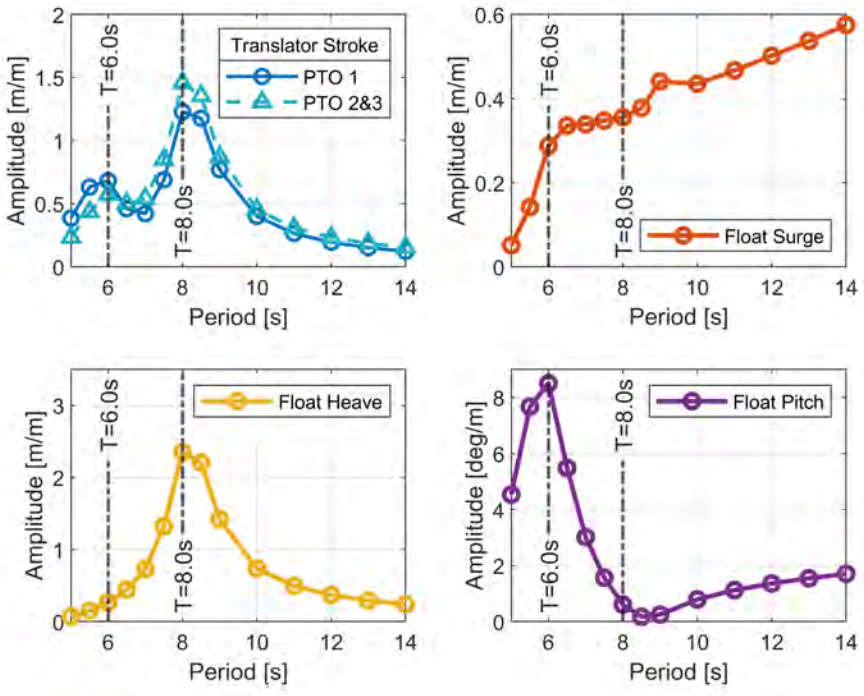

Figure 6.4: Three-Tether RAOs.

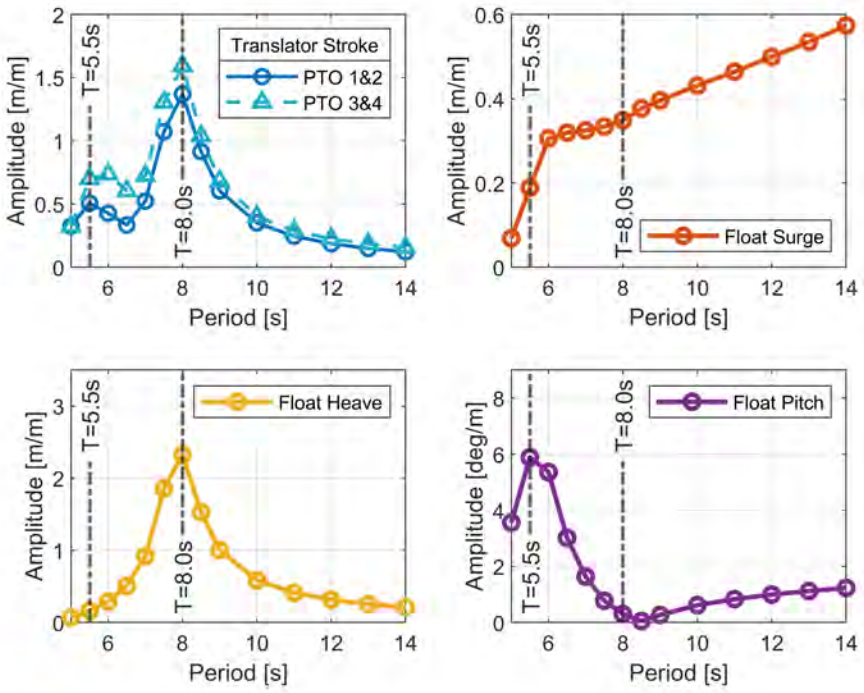

Figure 6.5: Four-Tether RAOs.

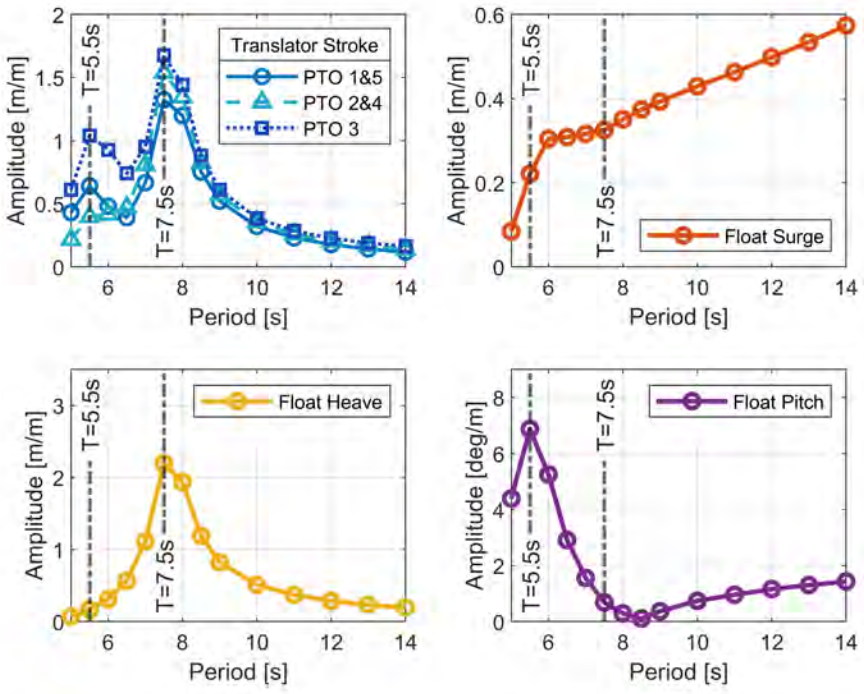

Figure 6.6: Five-Tether RAOs.

The single-tether configuration RAOs show only one primary peak translator response at 8.5 seconds, while all multi-tether configurations have both primary and secondary peaks. Each multi-tether's primary peak occurs around the same wave period as the single-tether and the secondary peak occurs at a shorter wave period. The amplitudes of their translator stroke responses also vary, the single-tether reaches 1.12, while the three-tether reaches 1.38 (average of the three translators), and the four-tether and the five-tether both reach 1.48 (average of their translators). The float heave RAO for all four configurations have a similar shape and their peaks coincide with the translator stroke peaks. Each reaches a value of around 2.34. A significant difference is seen in the surge and pitch RAOs between the single-tether and multi-tether configurations. The single-tether configuration's surge RAO has a gradually increasing response in surge as the wave period increases, but the multi-tether configurations see a rapid increase in their surge response around their secondary translator stroke peak response, before leveling off for a short interval before continuing to linearly increase to magnitudes slightly greater than that of the single-tether configuration. The single-tether configuration's pitch RAO is relatively steady across all wave periods, but the multi-tether configurations see a large spike at their secondary translator stroke peak responses, then drastically drop off to values lower than the single-tether configuration. Table 6.1 summarizes the trends observed from the RAO simulations.

Configuration	PP	Surge	Heave	Pitch	SP	Surge	Heave	Pitch
Single-Tether	8.5 s	↗	↑	→	None	—	—	—
Three-Tether	8.0 s	↗	↑	→	6.0 s	↑	↗	↑
Four-Tether	8.0 s	↗	↑	→	5.5 s	↑	↗	↑
Five-Tether	7.5 s	↗	↑	→	5.5 s	↑	↗	↑

↗ indicates a linear increasing trend, ↑ indicates a peak or steep increase, and → indicates a leveled off trend

Table 6.1: Trends in surge, heave, and pitch for each configuration's primary peak (PP) and secondary peak (SP) in translator stroke responses.

Damping Exhaustive Search

The results of the damping search are shown in figures 6.7a, 6.7c, 6.7b, and 6.7d for each respective configuration. Each plot shows the max instantaneous power plotted against the translator stroke. The color of each data point indicates the damping value. Note that the color bar scaling is a logarithmic scale, chosen to better differentiate the range in magnitude of damping values swept. The damping exhaustive search was done in two sweeps for each configuration, the first swept PTO damping values of 1e2, 1e3, 1e4, 1e5, 1e6, and 1e7 Ns/m to determine the magnitude around which the second sweep was conducted. Following the second sweep for all configurations, a clear peak in max instantaneous power was seen. The PTO damping value at that location was deemed optimal for the specified configuration.

Dotted lines indicate the cross-hair of maximum instantaneous power and the translator stroke value of the optimal damping value, the value of which is also labeled on each plot. The max instantaneous power reported for the multi-tether configurations is taken as the summation of each PTO's max instantaneous power.

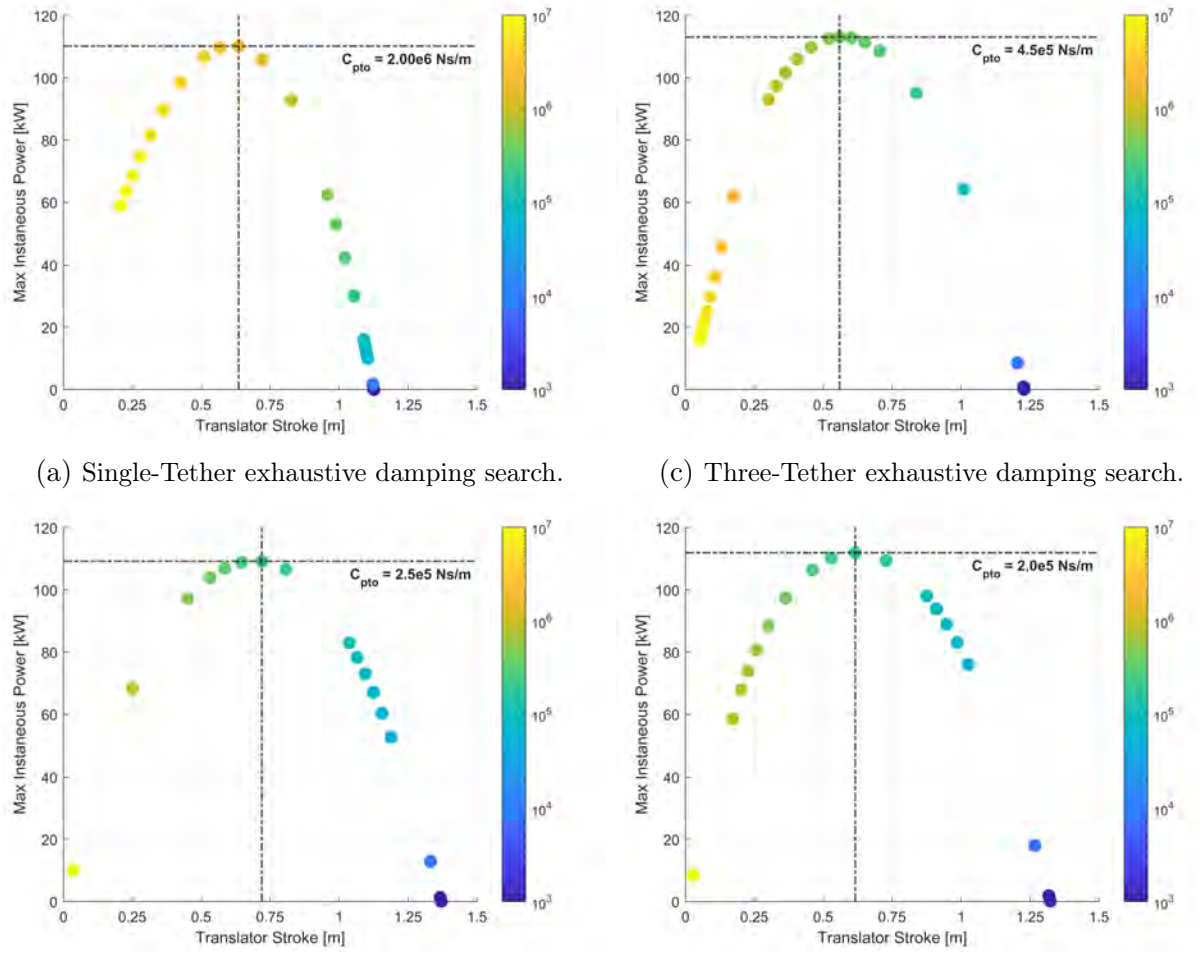

(a) Single-Tether exhaustive damping search.

(c) Three-Tether exhaustive damping search.

(b) Four-Tether exhaustive damping search.

(d) Five-Tether exhaustive damping search.

Figure 6.7: Exhaustive damping search comparison of the four configurations .

The optimal damping value for the single-tether configuration was determined to be 2.0 MNs/m, while all multi-tether configurations' optimal damping value was a magnitude smaller. A clear shift in the colors indicating the damping values around the peak in maximum instantaneous power is seen when comparing the single-tether to the multi-tether configurations. For all configurations, their peak in maximum instantaneous power occurs around a translator stroke range between 0.5 and 0.75 meters and reaches roughly the same value. The average maximum instantaneous peak power of the four configurations is 111 kilowatts. Table 6.2 summarizes the findings of the exhaustive damping search.

Configuration	Optimal C_{PTO}
Single-tether	2.0×10^6 N s/m
Three-tether	4.5×10^5 N s/m
Four-tether	2.5×10^5 N s/m
Five-tether	2.0×10^5 N s/m

Table 6.2: Optimal damping values.

6.3 Wave Simulations

Regular Waves

The results of the regular wave simulations for all four configurations, grouped by the wave period input are shown in Figure 6.8. For each configuration, the primary and secondary peak translator stroke responses from the RAO simulations are indicated. The yellow boxes with "P" indicate primary peaks and the green boxes with "S" indicate secondary peaks.

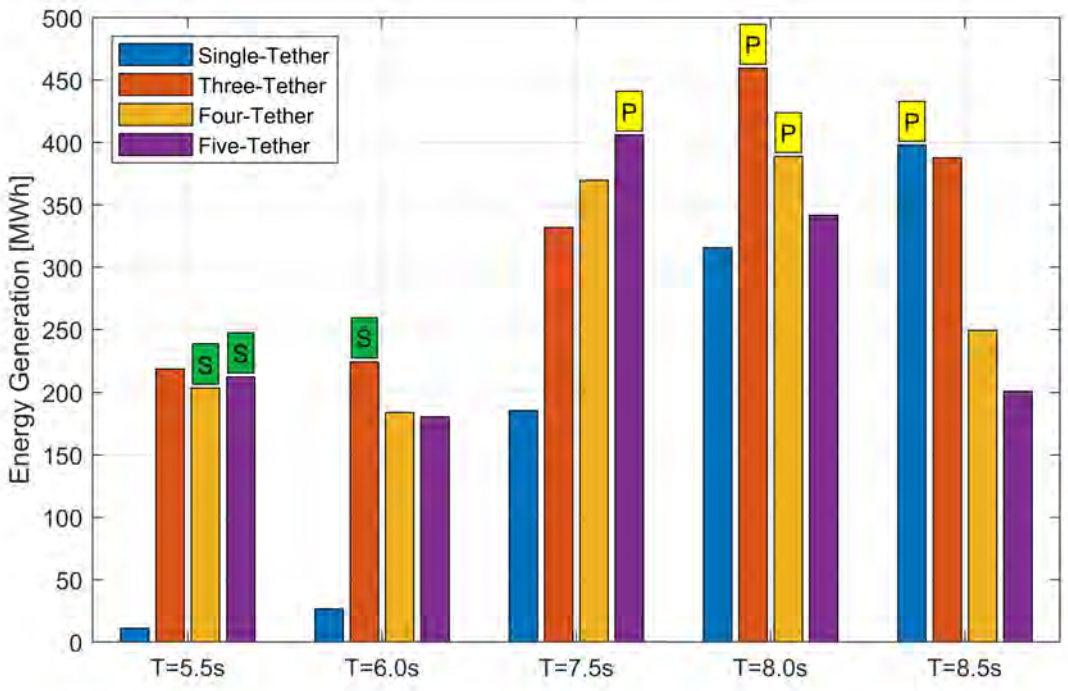

Figure 6.8: Regular Wave simulations run with a uniform wave height of 1.5 meters.

Each configuration has the greatest energy generation at its primary peak translator response in the range of selected wave periods. For the three-tether configuration, the energy generation at its secondary peak is greater than at a 5.5 second wave period, and for the four and five-tether configurations, the energy generation at their secondary peak is greater than

at a 6.0 second wave period. The multi-tether configurations far outperform the single-tether configuration at the shorter wave period of 5.5 and 6.0 seconds. An alternative plot of these results is shown in Figure 6.9 which highlights the three-tether configuration's broadband performance in comparison to other configurations. The plot is shown with continuous lines to help identify trends, but symbols indicate actual data points from simulations.

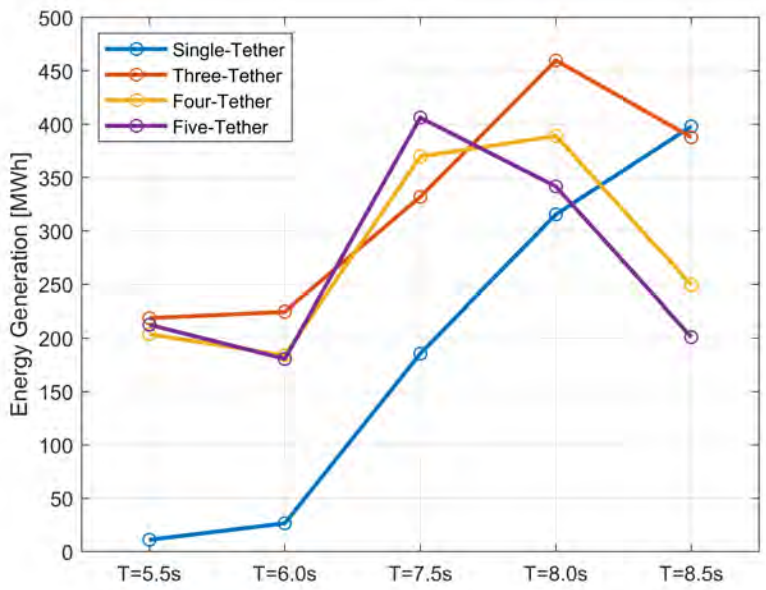

Figure 6.9: Regular Wave simulation energy generation trends with wave period.

Table 6.3 shows the energy generation of the multi-tether configurations compared to the single-tether configuration as a ratio.

Configuration	**Wave Period [s]**				
	5.5	6.0	7.5	8	8.5
Single-Tether	1.00	1.00	1.00	1.00	1.00
Three-Tether	19.76	8.46	1.79	1.46	0.97
Four-Tether	18.40	6.93	1.99	1.23	0.63
Five-Tether	19.2	6.81	2.19	1.08	0.50

Table 6.3: Energy generation comparison of multi-tether configurations to the single-tether configuration in regular waves.

Irregular Waves

A comparison of energy generation for all four configurations in irregular wave conditions, grouped by the location, is shown in Figure 6.10. The significant wave height, peak wave

period, and calculated wave resource at PacWave South, WETS, and Miami using Equation 2.7 are listed in Table 6.4 as a reference for the following series of plots.

Location	H_s	T_p	J_{irr}
PWS	1.5 m	9.88 s	14.85×10^3 W/m
WETS	1.5 m	7.56 s	11.36×10^3 W/m
MIA	0.75 m	5.00 s	1.38×10^3 W/m

Table 6.4: Wave resource at each location.

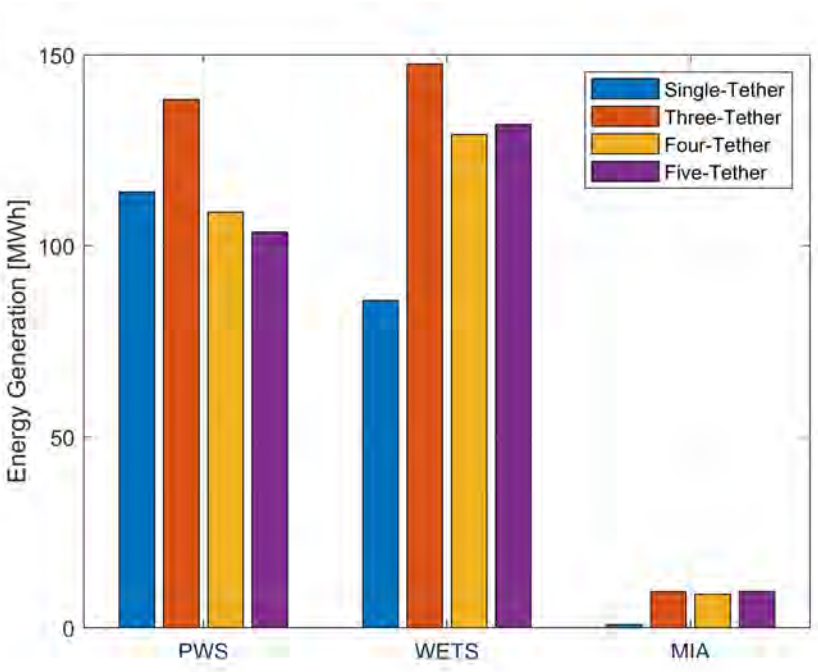

Figure 6.10: Irregular Wave simulations.

All locations were depicted on the same plot for ease of comparison, but the vast disparity in energy generation at PWS and WETS compared to Miami "hides" the energy generation of the single-tether configuration at the latter. The single-tether configuration does generate energy at this site but is on the order of kilowatt-hours in contrast to megawatt-hours generated by the multi-tether configurations. Overall, the three-tether configuration performs the best across the three selected wave climates, with only 0.1088 megawatt-hours fewer in energy generation in the Miami wave climate than the five-tether configuration. However, it is also apparent that this WEC, regardless of configuration, is far better suited for the PWS and WETS wave climates in terms of energy generation potential.

The tether tensions between the four configurations are also varied between configurations, most notably between the single-tether and multi-tether configurations. Figure 6.11 shows a comparison between the single-tether and three-tether configurations. Data from

the PWS irregular wave simulation is used as an example. WETS and Miami had similar magnitudes and trends to PWS, but are not shown here.

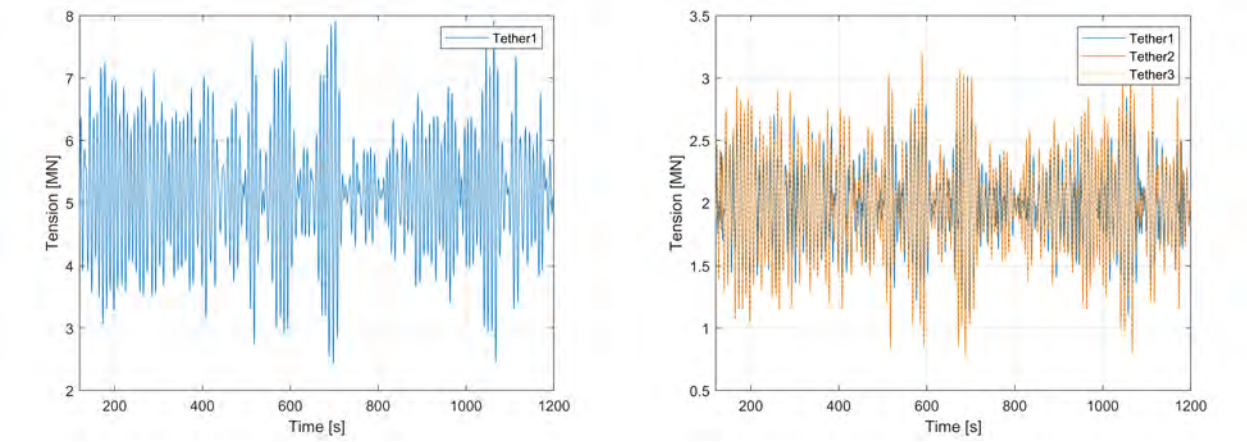

(a) Single-Tether tensions.

(b) Three-Tether tensions.

Figure 6.11: Tether tensions for single and three-tether configurations for the PWS simulations.

The single-tether's average tether tension is 5.17 MN, with a max value of 7.93 MN, while the three-tether averages 1.99 MN with a max value of 3.20 MN. Between the single-tether and three-tether configurations, there is a significant decrease in loading on the mooring system when additional tethers are added. By distributing the loading over two additional tethers the average tether tension is reduced by 61.5%. Figures 6.12 and 6.13 show the four and five-tether configurations.

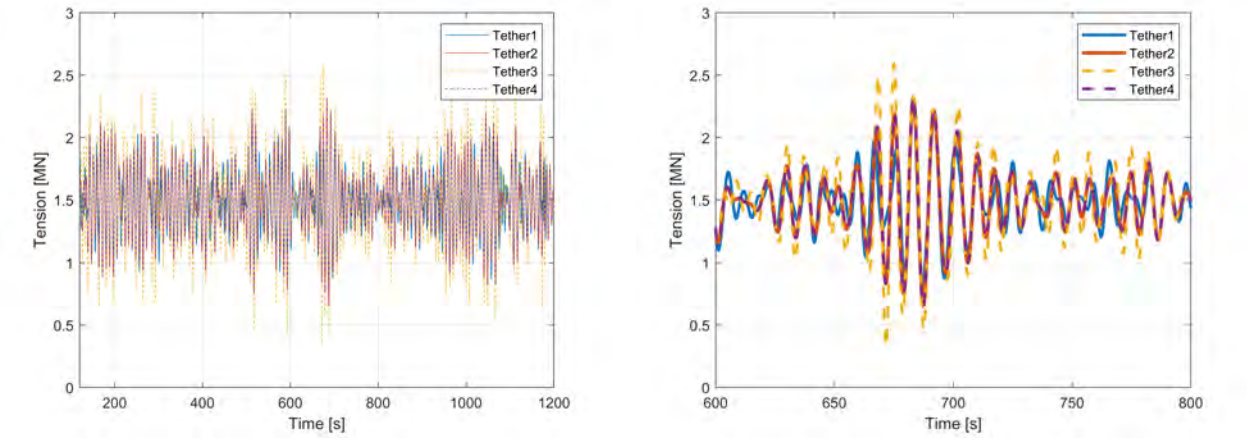

Figure 6.12: Tether tensions for the four-tether configuration (left) and enlarged view between 600 and 800 seconds (right).

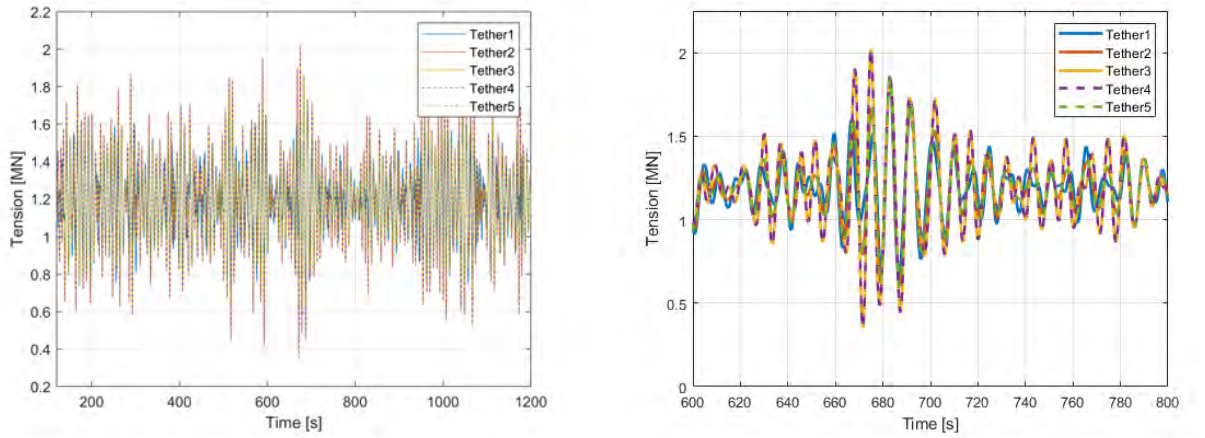

Figure 6.13: Tether tensions for the five-tether configuration (left) and enlarged view between 600 and 800 seconds (right).

The four-tether's average tether tension is 1.49 MN, with a max value of 2.74 MN, while the five-tether averages 1.19 MN with a max value of 2.12 MN. Adding additional tethers continues to decrease average and max values, which is expected with distributing the load, but the decrease is not linear and the greatest advantage is seen between the single-tether and three-tether. Table 6.5 displays a summary of the ratios of PTO stiffness, damping, average tether tension ($\overline{T_{ten}}$), and max tether tension (T_{max}) in relation to the single-tether configuration. This comparison shows a significant decrease in each between the single-tether and three-tether configurations, and then moderate decreases from three-tether to four and five-tether configurations.

Configuration	$\boldsymbol{K_{PTO}}$	$\boldsymbol{C_{PTO}}$	$\boldsymbol{\overline{T_{ten}}}$	$\boldsymbol{T_{max}}$
Single-Tether	1.00	1.00	1.00	1.00
Three-Tether	0.33	0.23	0.38	0.40
Four-Tether	0.25	0.13	0.29	0.35
Five-Tether	0.20	0.10	0.23	0.27

Table 6.5: Summary of PTO damping, stiffness, average tether tension, and max tether tension ratios.

The communication of PTO stiffness, PTO damping, and average tether tension is given as ratios to better focus on trends, rather than specific values. The significance of the reductions in values between configurations can only be truly quantified with appropriate economical analysis. However, it can be generally agreed upon that without considering the cost of adding each additional PTO and associated mooring equipment, reducing these values is favorable. The PTO stiffness and PTO damping magnitudes can be understood to have an influence on the size and capacity of the PTO required. Reducing tether tensions in

terms of average and max values can also be understood to influence the mooring material selection and sizing.

COV

A comparison of COV for all four configurations, grouped by the location, is shown in Figure 6.14. Note, a higher COV value indicates poorer power quality.

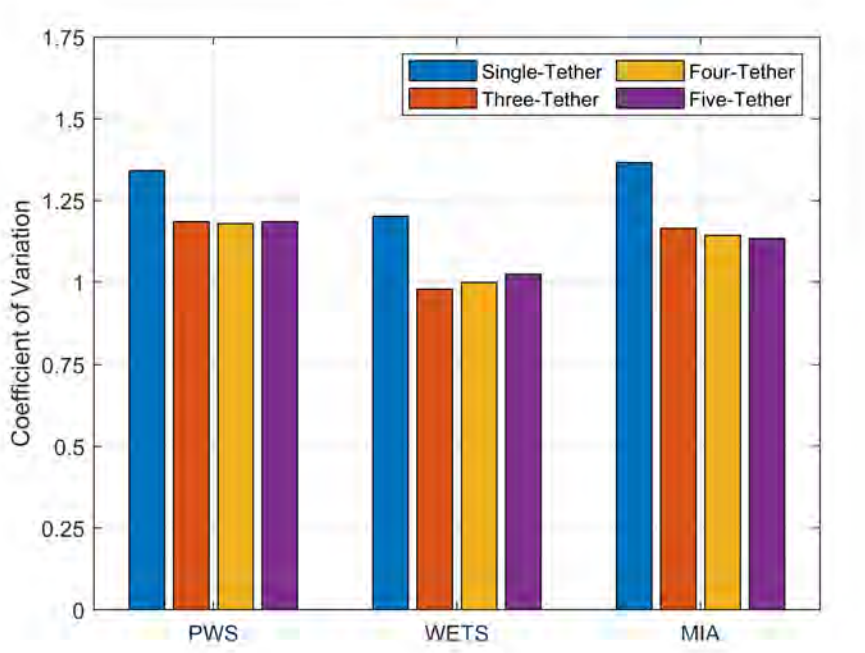

Figure 6.14: COV comparison of configurations from irregular wave simulations.

Relatively small ranges in COV between configurations are seen for the selected wave conditions, with only notable differences between the single-tether configuration versus the multi-tether configurations. For all locations, the single-tether configuration has poorer power quality in terms of COV.

CWR

A comparison of CWR for all four configurations, grouped by the location, is shown in Figure 6.15. The characteristic dimension is the same for all four configurations (B = 25 meters). As the coupled PTO-mooring configuration changes, the same diameter is used to calculate CWR as each uses the same float.

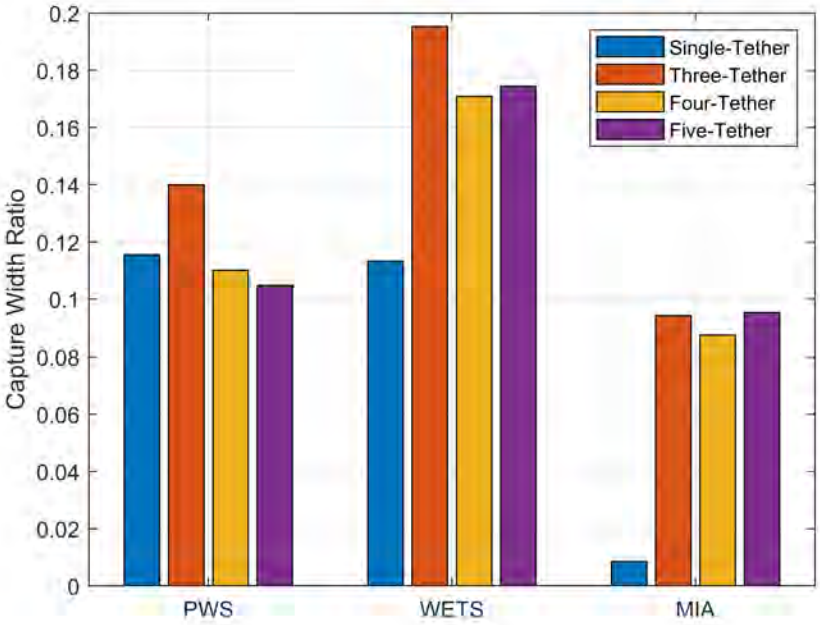

Figure 6.15: CWR comparison of configurations from irregular wave simulations.

The effect of treating each configuration as having the same characteristic dimension (same float diameter) regardless of the footprint of its mooring system is that this plot largely reflects the previous energy generation plot in Figure 6.10. Similarly, the three-tether configuration performs the best overall across the three selected wave climates. However, the CWR highlights that although there is a small wave resource in the Miami climate, the multi-tether configurations show hydrodynamic efficiencies more comparable to PacWave South and WETS, than seen when looking at purely energy generation in Figure 6.10.

Wave Energy Decay Simulations

Figure 6.16 shows the energy generation plotted against the depth of submergence. An alternative perspective of this same data is shown in Figure 6.17 with the depth of submergence (left y-axis) and the ratio of the depth of submergence to wavelength (right y-axis) plotted against the energy generation ratio. The energy generation ratio for each configuration is defined as the energy generation at each specified depth of submergence divided by the energy generation of the configuration at 6.5 meters submerged (baseline). The wave orbital motion decay is also plotted using e^{-kd_s}, the scaling factor from Equation 2.4, also scaled to the orbital trajectory at 6.5 meters (baseline) to provide a ratio. Plots are shown with continuous lines to help identify trends, but symbols indicate actual data points from simulations.

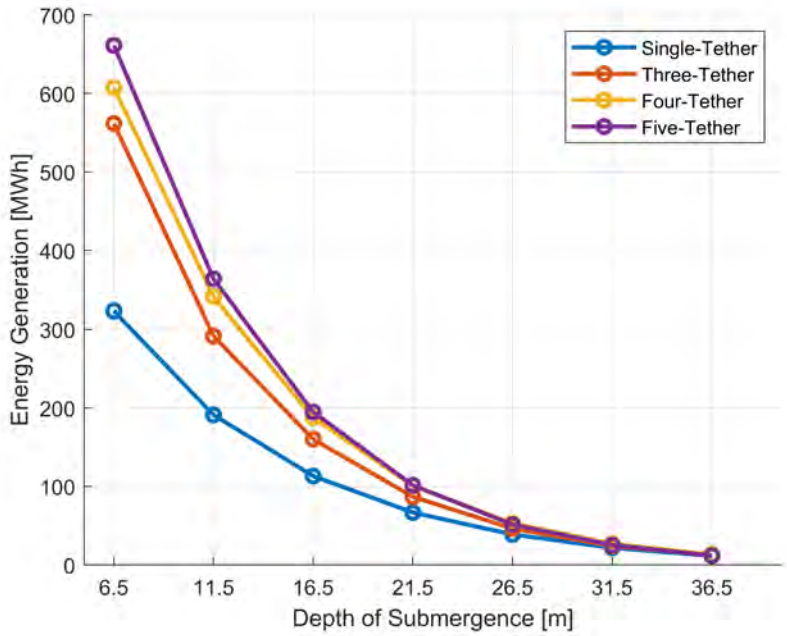

Figure 6.16: Energy generation comparison of configurations run with regular waves with H = 2 m & T = 7.5 s.

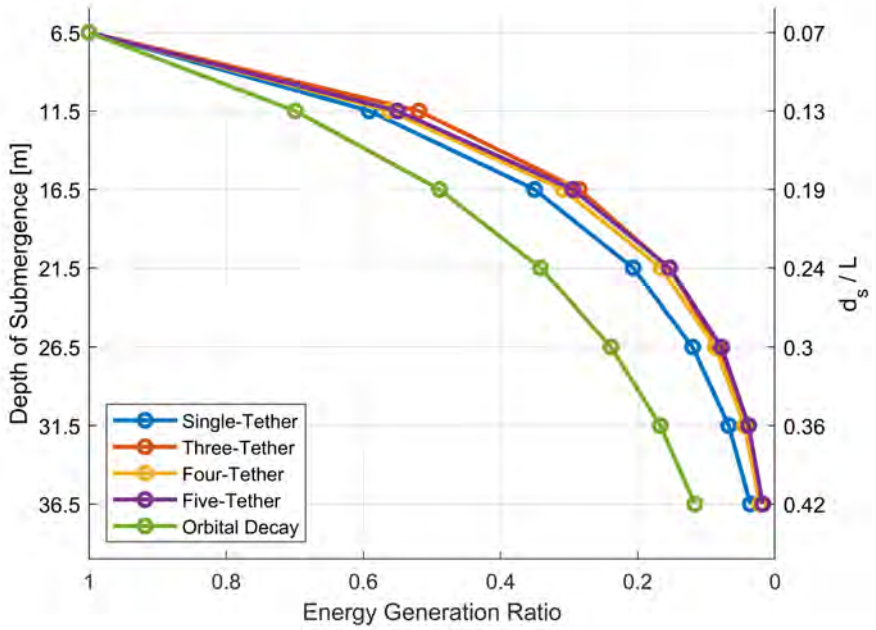

Figure 6.17: Energy generation ratio decay comparison of configurations run with regular waves with H = 2 m & T = 7.5 s.

Figure 6.16 illustrates how each configuration starts at different energy generation values,

but all exponentially decrease to roughly the same value at 36.5 meters submerged from the still water line. The actual energy generation value at the baseline for each configuration is not as relevant in this analysis as this is largely dependent on the selected wave condition. From theory, at a depth of half the wavelength, there is negligible water movement and any size float with any mooring configuration is expected to decay to zero at approximately 43.9 meters below the water surface for this specific wave condition. Figure 6.17 shows that all four configurations follow the same trend in energy generation ratio decay, which matches the shape of the expected wave orbital motion decay. The multi-tether configurations track closely together, and the single-tether configuration shows a slightly slower decay in its energy generation ratio. However, it is worth noting that the single-tether shows significantly less energy generation at this wave condition in comparison to the multi-tether configuration and its appearance of slower decay may be more from the effect of showing all configurations on the same plot than a performance advantage.

Chapter 7

Discussion

The following sections provide further examination of observations made during the analysis. Section 7.1 discusses the implications of some of the modeling choices. Section 7.2 expands on the possible contributing factors to the differences in RAOs between configurations. Section 7.3 ties together the wave simulations' findings and provides an overall evaluation of the four configurations.

7.1 ProteusDS Modeling

The case study WEC was built within the capabilities and limitations of the chosen modeling software, ProteusDS, and drew upon guidance found in the available literature. Modeling choices were made, and their implications can be considered. However, for this study whose aim was to compare different WEC configurations, consistent parameters, and a methodical process to determine the layout of multi-tether configurations seems the most vital. The choice to use ProteusDS' Rigid Body Cylinder feature to model the WEC float, rather than obtaining hydrodynamic coefficients from a boundary element method (BEM) solver from a custom meshed geometry is presumably the most impactful. However, this choice was made as a balance between using a method that involved only one proprietary software versus four, reducing the computational cost to carry out more simulations, and no real need to analyze a complex float geometry, but at the cost of neglecting radiation damping and diffraction effects. The inclusion of these effects would undoubtedly improve the accuracy of the model, but may not be as important when only considering the comparison of performance between models that all neglect these effects. However, neglecting radiation damping effects could lead to an overestimation of float motions, and in turn, translator oscillation and calculated mechanical power. When the float is excited by the incoming waves, some of the energy is converted into radiated waves from the body's motion and lost. Neglecting wave diffraction in the model means that waves are not altered as they pass

the body, and the bending or spreading of the waves is not calculated or tracked. Wave diffraction may create wave interactions on the leeward side. This alteration of the wave field is not as impactful, relative to other effects in the equation of motion, but may be more relevant for WEC arrays.

The PTO model also diverged from literature descriptions in the implementation of the retracting springs creating the restoring force needed for a submerged WEC. Multiple publications included a constant value (not dependent on displacement), labeled a pretension value, and were included in the PTO force calculation that balanced out the float's buoyancy. However, the implementation of the restoring force in this methodology was to include a spring stiffness in the PTO joint which is the only option in ProteusDS. This modeling choice, as emphasized before, makes the restoring force dependent on displacement. The reduction in PTO stiffness from those supposed by literature is most likely tied to this modeling choice. As the translator moved past the equilibrium position where the PTO force and buoyancy force was balanced, any additional displacement increased the PTO force to a value too large which overly restricted the translator's oscillations. If a model could include a constant value, the PTO force would not increase with displacement and would presumably allow normal oscillations of the translator. For envisioned future experimental testing of a scaled prototype, the restoring force is set to be implemented with an external air spring which will not be part of the PTO system but will be dependent on displacement. With this consideration, modeling the PTO with the methodology presented in earlier sections seems the most appropriate modeling method.

The placement of PTO at the seafloor, rather than inside the float itself was also a modeling choice. This was based on the restrictions to implement a PTO in ProteusDS' environment. If the setup was reversed and the PTOs were placed inside the float and tethers were anchored directly to the seafloor to provide a reaction point for the WEC there is no expected impact to the WEC hydrodynamics. However, the mass of the float would need to be adjusted to account for the mass of the PTOs, and PTOs would need to be placed fully inside the float so that their components do not interfere with the fluid dynamics around the float's boundary. Ideally, the PTO would be modified to a rotary PTO so that the equivalent linear PTO translator stroke could be maintained.

7.2 Preliminary Simulations

The RAO simulations' major finding was secondary peak translator responses for multi-tether configurations, but only one peak for the single-tether configuration. Trends in surge, heave, and pitch were identified in the results section, and further explanation for this behavior is now discussed. From the analysis of the visualization output from ProteusDS, it is seen that the multi-tether configurations are pitch dominated with little heave response

at shorter wave periods, then the float stabilizes with virtually no pitching at longer wave periods, transitioning almost entirely into heave. Their pitch response and contribution from surge appear to allow multi-tether configurations to gain this secondary peak at short wave periods. This behavior is not seen for the single-tether, which has a relatively steady pitch response at all simulated wave periods.

The damping exhaustive search's major finding was that a single-tether configuration requires significantly larger PTO damping compared to the multi-tether configuration. Overall, this is not unexpected, but it carries implications for the needed capacity of a single PTO. The capital expenditure for each system is not a part of this study, but it is a broad factor for consideration when deciding between a single or multi-tether configuration for a WEC design that involves a coupled PTO-mooring system. The relevance of the reduction in PTO damping, as well as PTO stiffness, can only be quantified with an appropriate analysis of the economics.

7.3 Wave Simulations

The regular wave simulations largely followed the RAO simulations. However, the expectation of adding PTO damping would have been for the resonant period to shift to lower frequencies. For each configuration, each showed the best performance at its respective peak translator frequency identified during the RAO simulations. However, regular waves are not representative of real sea states, therefore irregular wave conditions were also run to bolster the validity of the findings.

The irregular wave cases broadly showed that the multi-tether configurations perform better than the single-tether at shorter peak wave periods, and conversely, the single-tether performs better, but not the best, at longer wave periods. In terms of energy generation, the three-tether configuration showed the best performance in the three selected wave climates on the whole. The multi-tether configurations far outperform the single-tether at WETS and Miami, with a peak period of 7.56 seconds and 5.00 seconds, respectively. In terms of tether tension, the addition of tethers significantly reduces the loading on individual tethers, most notably between the single to the three-tether case. COV showed a slight advantage towards multi-tether over single-tether. In all cases, the standard deviation of the instantaneous power roughly meets or exceeds the mean of the instantaneous power (i.e. each COV is approximately equal to 1 or of greater magnitude) which suggests that a power smoothing method would still be needed as each was greater than one or near unity. The CWR, which largely reflected the energy generation comparison as all were normalized by the float's 25-meter diameter, showed again that the three-tether configuration had the best performance in the three selected wave climates on the whole. As the climate with the closest values, a summary of the PacWave South findings is provided in Table 7.1 for ease of holistic

comparison.

Configuration	C_{PTO}	E_{gen}	$\overline{T_{tens}}$	COV	CWR
Single-Tether	2.0×10^6 N s/m	114.13 MW h	5.17 MN	1.34	1.12
Three-Tether	4.5×10^5 N s/m	138.33 MW h	1.99 MN	1.18	1.14
Four-Tether	2.5×10^5 N s/m	108.80 MW h	1.49 MN	1.17	1.11
Five-Tether	2.0×10^5 N s/m	103.61 MW h	1.19 MN	1.18	1.10

Table 7.1: Summary of findings from the PWS irregular wave simulations.

Additionally, a table of energy generation, COV, and CWR ratios to the single-tether configuration for PacWave South, WETS, and Miami is shown below in Figure 7.2. Ratios are in comparison to the single-tether configuration and are calculated by dividing each value by the single-tether's performance (i.e. the single-tether is 1.00 in all cases, and the multi-tether configurations show the scaling to the single-tether's value). Green highlighted cells show the best-performing configuration. Note, for COV, a smaller value shows better power quality.

Configuration	PWS			WETS			MIA		
	E_{gen}	COV	CWR	E_{gen}	COV	CWR	E_{gen}	COV	CWR
Single-Tether	1.00	1.00	1.00	1.00	1.00	1.00	1.00	1.00	1.00
Three-Tether	1.21	0.88	1.21	1.72	0.81	1.72	11.05	0.85	11.08
Four-Tether	0.95	0.88	0.95	1.51	0.83	1.51	10.28	0.84	10.32
Five-Tether	0.91	0.88	0.91	1.54	0.85	1.54	11.18	0.83	11.21

Table 7.2: Summary of energy generation, COV, and CWR ratios.

From a review of the power performance metrics presented above, adding additional tethers to capture energy in more modes, i.e. surge, and pitch, improves power performance. However, the use of more than three tethers seems redundant in terms of adding to energy capture in more modes and generally shows less energy generation and no significant improvement in power quality. The five-tether configuration only slightly outperforms the three-tether configuration in the Miami climate. However, the three-tether configuration shows superior performance at PacWave South and WETS in comparison to the other configurations in consideration of the calculated metrics.

The wave energy decay simulations confirmed general expectations from the theory. They also provided a comparison of how each configuration is affected by deeper submergence. The multi-tether configurations decay similarly and the single-tether configuration appears to decay slightly slower. However, overall no significant difference is apparent with different mooring configurations and their trends follow that of the wave orbital decay. In addition, the single-tether's slightly slower decay is overshadowed by the fact that it generates far less energy than the multi-tether configurations at the simulated wave period.

Chapter 8

Conclusion

The main objective of this thesis was to answer two research questions regarding subsurface WECs:

RESEARCH QUESTION 1 (RQ1). How does the number of tethers in a coupled power take-off mooring system affect power performance in a subsurface WEC?

RESEARCH QUESTION 2 (RQ2). How does the energy generation decay with increasing submergence depths for WECs with different mooring system configurations?

The results of this study showed that the number of tethers in a coupled PTO-mooring system highly affects energy generation and influences power quality. However, simply adding additional PTOs does not increase energy generation. Rather, the three-tether configuration appears to make the best use of increased modes of energy capture, and the addition of more PTOs does not result in significant gains and may lead to less energy generation. Power quality is improved with the addition of tethers and PTOs as the instantaneous power from each PTO in the multi-tether configurations is slightly offset from one another. PTO stiffness, PTO damping, average tether tensions, and max tether tensions are also reduced with additional tethers and PTOs. To reiterate, these reductions are not unexpected, but they are not linearly decreasing, with the greatest improvements between the single and three-tether configurations. Without consideration of the economical implications of adding two additional PTOs and tethers, the three-tether configuration results suggest it is the best choice.

For the different configurations, analysis using regular waves with the selected wave condition showed that each decays similarly with depth. There is not a significant difference between configurations. However, the main takeaway is that each, regardless of their energy generation near the surface, is expected to decay to virtually zero, by theory, around a depth

of half the wavelength. Additionally, the configurations roughly follow the orbital wave decay with depth, and different tuning may bring energy generation ratios closer to the magnitude of the orbital decay but is not expected to change the overall exponential decaying trend.

Future work furthering this study is the reiteration of this analysis using the set framework with the inclusion of wave radiation damping and wave diffraction effects. This could be accomplished by creating a CAD design of the float, meshing the geometry in appropriate software, and obtaining the hydrodynamic coefficients from a BEM solver. In addition, other parameters could be explored such as float aspect ratio, different shapes, tether attachment point, tether inclination angle, float mass, and float center of gravity. These parameters often show dependency on each other so their investigation per case study is often needed as publications have scopes limited to their specific cases. The PTO damping and stiffness could also be improved with an optimization study to find truly optimal values. Finally, an investigation of how the performance of the different configurations in intermediate and shallow water could be analyzed. As the relative water depth decreases, wave orbitals change shape from circular to elliptical shaped trajectories. This change in shape could show significant effects on energy capture modes, especially in surge.

This study has created a framework for modeling subsurface WECs in ProteusDS which has been made adaptable to support future work in subsurface WEC research. The results of this analysis for the chosen case study have been presented, with the limitations and caveats to specific values stated. The trends in behavior and general characterization of each configuration are highlighted as the most significant contribution to future researchers. This work may reflect Carnegie Clean Energy's move from the CETO 5, a single-tether design, to the CETO 6, a three-tether design, however further investigation of this type of design in different wave conditions, and relative water depths is recommended to fully understand the implications of adding additional tethers and PTOs. For the marine energy sector as a whole, this research seeks to support the advancement of subsurface WECs and the design, build, and testing of a scaled prototype in the O.H. Hinsdale Wave Research Laboratory at Oregon State University.

Bibliography

[1] Anthony Lewis et al. "Ocean Energy". en. In: *IPCC Special Report on Renewable Energy Sources and Climate Change Mitigation*. Ocean Energy. Cambridge, United Kingdom and New York, NY, USA: Cambridge University Press, 2011, pp. 497–533. URL: https://www.ipcc.ch/site/assets/uploads/2018/03/Chapter-6-Ocean-Energy-1.pdf.

[2] *IRENA Ocean Energy Technology Brief 4*. en. Tech. rep. 2014.

[3] *Ocean Energy — IPCC*. URL: https://www.ipcc.ch/report/renewable-energy-sources-and-climate-change-mitigation/ocean-energy/ (visited on 06/01/2023).

[4] Alain Clément et al. "Wave energy in Europe: current status and perspectives". en. In: *Renewable and Sustainable Energy Reviews* 6.5 (Oct. 2002), pp. 405–431. ISSN: 13640321. DOI: 10.1016/S1364-0321(02)00009-6. URL: https://linkinghub.elsevier.com/retrieve/pii/S1364032102000096 (visited on 05/04/2023).

[5] Duarte Valério, Pedro Beirão, and José Sá Da Costa. "Optimisation of wave energy extraction with the Archimedes Wave Swing". en. In: *Ocean Engineering* 34.17-18 (Dec. 2007), pp. 2330–2344. ISSN: 00298018. DOI: 10.1016/j.oceaneng.2007.05.009. URL: https://linkinghub.elsevier.com/retrieve/pii/S0029801807001436 (visited on 05/04/2023).

[6] Raju Ahamed, Kristoffer McKee, and Ian Howard. "Advancements of wave energy converters based on power take off (PTO) systems: A review". en. In: *Ocean Engineering* 204 (May 2020), p. 107248. ISSN: 00298018. DOI: 10.1016/j.oceaneng.2020.107248. URL: https://linkinghub.elsevier.com/retrieve/pii/S0029801820302985 (visited on 05/04/2023).

[7] *Carnegie Clean Energy Annual Report 2018*. Tech. rep. 2018. URL: https://www.asx.com.au/asxpdf/20181019/pdf/43zfn5j2k90pk1.pdf.

[8] Christophe Gaudin et al. "A Wave Energy Research Centre in Albany, Australia". en. In: *Proceedings of the 4th Asian Wave and Tidal Energy Conference* (2018). URL: https://tethys-engineering.pnnl.gov/sites/default/files/publications/AWTEC2018-371.pdf.

[9] Baba Tamim. *'Archimedes Waveswing': 20 years of research leads to successful trials of this wave energy converter*. en-US. Nov. 2022. URL: https://interestingengineering.com/innovation/archimedes-waveswing-successful-trail (visited on 06/01/2023).

[10] *Technology – Symphony Wave Power*. en-US. URL: https://symphonywavepower.nl/technology/ (visited on 06/01/2023).

[11] https://www.abc.net.au/news/kathryn-diss/4960710 and https://www.abc.net.au/news/rebecca-turner/7053638. "Waves of discontent as storm hits Perth-based renewable energy darling". en-AU. In: *ABC News* (Sept. 2018). URL: https://www.abc.net.au/news/2018-09-22/power-company-carnegie-energy-hit-by-wave-of-discontent/10289772 (visited on 06/01/2023).

[12] Amir Garanovic. *CalWave commissions wave energy pilot offshore California*. en-US. Oct. 2021. URL: https://www.offshore-energy.biz/calwave-commissions-wave-energy-pilot-offshore-california/ (visited on 06/01/2023).

[13] Arthur Pecher and Jens Peter Kofoed, eds. *Handbook of Ocean Wave Energy*. en. Vol. 7. Ocean Engineering & Oceanography. Cham: Springer International Publishing, 2017. ISBN: 978-3-319-39888-4 978-3-319-39889-1. DOI: 10.1007/978-3-319-39889-1. URL: http://link.springer.com/10.1007/978-3-319-39889-1 (visited on 05/04/2023).

[14] *Overview — WEC-Sim documentation*. URL: https://wec-sim.github.io/WEC-Sim/dev/theory/theory.html#regular-waves (visited on 05/25/2023).

[15] Dynamic Systems Analysis Ltd. *ProteusDS 2015 Manual*. URL: https://dsaocean.com/downloads/documentation/ProteusDS%202015%20Manual.pdf.

[16] Wanan Sheng and Anthony Lewis. "Assessment of Wave Energy Extraction From Seas: Numerical Validation". en. In: *Journal of Energy Resources Technology* 134.4 (Dec. 2012), p. 041701. ISSN: 0195-0738, 1528-8994. DOI: 10.1115/1.4007193. URL: https://asmedigitalcollection.asme.org/energyresources/article/doi/10.1115/1.4007193/372886/Assessment-of-Wave-Energy-Extraction-From-Seas (visited on 05/05/2023).

[17] Shaohui Yang et al. "Modelling and analysis of inertia self-tuning phase control strategy for a floating multi-body wave energy converter". In: *IET Renewable Power Generation* (2021). DOI: 10.1049/rpg2.12208.

[18] Robert G. Dean and Robert A. Dalrymple. *Water Wave Mechanics for Engineers and Scientists*. Vol. 2. Advanced Series on Ocean Engineering. 1984.

[19] Gerhard Masselink. "Waves". en. In: *Encyclopedia of Coastal Science*. Ed. by Charles W. Finkl and Christopher Makowski. Series Title: Encyclopedia of Earth Sciences Series. Cham: Springer International Publishing, 2019, pp. 1878–1886. ISBN: 978-3-319-93805-9 978-3-319-93806-6. DOI: 10.1007/978-3-319-93806-6_350. URL: https://link.springer.com/10.1007/978-3-319-93806-6_350 (visited on 06/01/2023).

[20] John V. Ringwood, Giorgio Bacelli, and Francesco Fusco. "Energy-Maximizing Control of Wave-Energy Converters: The Development of Control System Technology to Optimize Their Operation". en. In: *IEEE Control Systems* 34.5 (Oct. 2014), pp. 30–55. ISSN: 1066-033X, 1941-000X. DOI: 10.1109/MCS.2014.2333253. URL: https://ieeexplore.ieee.org/document/6898109/ (visited on 05/04/2023).

[21] Jeremiah Pastor and Yucheng Liu. "Wave Climate Resource Analysis Based on a Revised Gamma Spectrum for Wave Energy Conversion Technology". en. In: *Sustainability* 8.12 (Dec. 2016), p. 1321. ISSN: 2071-1050. DOI: 10.3390/su8121321. URL: http://www.mdpi.com/2071-1050/8/12/1321 (visited on 05/05/2023).

[22] Nicolas Guillou. "Estimating wave energy flux from significant wave height and peak period". en. In: *Renewable Energy* 155 (Aug. 2020), pp. 1383–1393. ISSN: 09601481. DOI: 10.1016/j.renene.2020.03.124. URL: https://linkinghub.elsevier.com/retrieve/pii/S0960148120304560 (visited on 05/08/2023).

[23] Bryson Robertson et al. "Influence of wave resource assessment methodology on wave energy production estimates". en. In: *Renewable Energy* 86 (Feb. 2016), pp. 1145–1160. ISSN: 09601481. DOI: 10.1016/j.renene.2015.09.020. URL: https://linkinghub.elsevier.com/retrieve/pii/S0960148115302998 (visited on 05/25/2023).

[24] W.E. Cummins. *The Impulse Response Function and Ship Motion*. Tech. rep. 1962. URL: https://repository.tudelft.nl/islandora/object/uuid:222ffea6-85c2-4e34-ad69-bddfaa750081/datastream/OBJ/download.

[25] M. Folley. *NUMERICAL MODELLING OF WAVE ENERGY CONVERTERS*. en. Elsevier, 2016. ISBN: 978-0-12-803210-7. DOI: 10.1016/B978-0-12-803210-7.00001-3. URL: https://linkinghub.elsevier.com/retrieve/pii/B9780128032107000013 (visited on 05/04/2023).

[26] Dezhi Ning and Boyin Ding. *Modelling and Optimisation of Wave Energy Converters*. en. 1st ed. Boca Raton: CRC Press, July 2022. ISBN: 978-1-00-319895-6. DOI: 10.1201/9781003198956. URL: https://www.taylorfrancis.com/books/9781003198956 (visited on 05/04/2023).

[27] J.R. Morison, J.W. Johnson, and S.A. Schaaf. "The Force Exerted by Surface Waves on Piles". en. In: *Journal of Petroleum Technology* 2.05 (May 1950), pp. 149–154. ISSN: 0149-2136, 1944-978X. DOI: 10.2118/950149-G. URL: https://onepetro.org/JPT/article/2/05/149/161931/The-Force-Exerted-by-Surface-Waves-on-Piles (visited on 05/04/2023).

[28] *ProteusDS*. Feb. 2021.

[29] *ProteusDS Tutorials — ProteusDS Documentation 2.49.0 documentation*. URL: http://documentation.dsaocean.com/tutorials/ (visited on 05/24/2023).

[30] Bingyong Guo and John V. Ringwood. "A review of wave energy technology from a research and commercial perspective". en. In: *IET Renewable Power Generation* 15.14 (Oct. 2021), pp. 3065–3090. ISSN: 1752-1416, 1752-1424. DOI: 10.1049/rpg2.12302. URL: https://onlinelibrary.wiley.com/doi/10.1049/rpg2.12302 (visited on 05/04/2023).

[31] K. Budar and J. Falnes. "A resonant point absorber of ocean-wave power". en. In: *Nature* 256.5517 (Aug. 1975), pp. 478–479. ISSN: 0028-0836, 1476-4687. DOI: 10.1038/256478a0. URL: https://www.nature.com/articles/256478a0 (visited on 05/27/2023).

[32] B Drew, A R Plummer, and M N Sahinkaya. "A review of wave energy converter technology". en. In: *Proceedings of the Institution of Mechanical Engineers, Part A: Journal of Power and Energy* 223.8 (Dec. 2009), pp. 887–902. ISSN: 0957-6509, 2041-2967. DOI: 10.1243/09576509JPE782. URL: http://journals.sagepub.com/doi/10.1243/09576509JPE782 (visited on 05/04/2023).

[33] Johannes Falnes and Jørgen Hals. "Heaving buoys, point absorbers and arrays". en. In: *Philosophical Transactions of the Royal Society A: Mathematical, Physical and Engineering Sciences* 370.1959 (Jan. 2012), pp. 246–277. ISSN: 1364-503X, 1471-2962. DOI: 10.1098/rsta.2011.0249. URL: https://royalsocietypublishing.org/doi/10.1098/rsta.2011.0249 (visited on 05/04/2023).

[34] Johannes Falnes and Jørgen Løvseth. "Ocean wave energy". en. In: *Energy Policy* 19.8 (Oct. 1991), pp. 768–775. ISSN: 03014215. DOI: 10.1016/0301-4215(91)90046-Q. URL: https://linkinghub.elsevier.com/retrieve/pii/030142159190046Q (visited on 05/27/2023).

[35] António F. De O. Falcão. "Wave energy utilization: A review of the technologies". en. In: *Renewable and Sustainable Energy Reviews* 14.3 (Apr. 2010), pp. 899–918. ISSN: 13640321. DOI: 10.1016/j.rser.2009.11.003. URL: https://linkinghub.elsevier.com/retrieve/pii/S1364032109002652 (visited on 05/04/2023).

[36] Linus Mofor, Jarett Goldsmith, and Fliss Jones. *IRENA Ocean Energy Report*. Tech. rep. 2014.

[37] Tunde Aderinto and Hua Li. "Review on Power Performance and Efficiency of Wave Energy Converters". en. In: *Energies* 12.22 (Nov. 2019), p. 4329. ISSN: 1996-1073. DOI: 10.3390/en12224329. URL: https://www.mdpi.com/1996-1073/12/22/4329 (visited on 05/08/2023).

[38] Iraide López et al. "Review of wave energy technologies and the necessary power-equipment". en. In: *Renewable and Sustainable Energy Reviews* 27 (Nov. 2013), pp. 413–434. ISSN: 13640321. DOI: 10.1016/j.rser.2013.07.009. URL: https://linkinghub.elsevier.com/retrieve/pii/S1364032113004541 (visited on 05/28/2023).

[39] Tunde Aderinto and Hua Li. "Ocean Wave Energy Converters: Status and Challenges". en. In: *Energies* 11.5 (May 2018), p. 1250. ISSN: 1996-1073. DOI: 10.3390/en11051250. URL: http://www.mdpi.com/1996-1073/11/5/1250 (visited on 05/04/2023).

[40] awsoceanwebmaster. *AWS Waveswing trials exceed expectations*. en-GB. Nov. 2022. URL: https://awsocean.com/2022/11/aws-waveswing-trials-exceed-expectations/ (visited on 05/24/2023).

[41] *Symphony Wave Power – The new wave of invisible energy*. URL: https://symphonywavepower.nl/ (visited on 05/27/2023).

[42] *Carnegie CETO 6 Technology*. en-AU. URL: https://arena.gov.au/projects/carnegie-ceto-6-technology/ (visited on 06/07/2022).

[43] *CalWave Successfully Commissioned Open-Water Wave Energy Pilot – CalWave*. en-US. URL: https://calwave.energy/full-press-release-calwave-successfully-commissioned-open-water-wave-energy-pilot/ (visited on 06/01/2023).

[44] Pasquale Filianoti and Sergio M. Camporeale. "A linearized model for estimating the performance of submerged resonant wave energy converters". en. In: *Renewable Energy* 33.4 (Apr. 2008), pp. 631–641. ISSN: 09601481. DOI: 10.1016/j.renene.2007.03.018. URL: https://linkinghub.elsevier.com/retrieve/pii/S0960148107001012 (visited on 05/04/2023).

[45] Mike Morrow. *DMP: SIMPLE, SCALABLE AND SUBMERGED M3 WAVE ENERGY SYSTEMS LLC*. Tech. rep. 2011.

[46] *mWave™ | Bombora*. URL: https://bomborawave.com/mwave/ (visited on 06/01/2023).

[47] Ryan Coe et al. *FOSWEC dynamics and controls test report*. en. Tech. rep. SAND–2020-11695, 1717884, 692227. Oct. 2020, SAND–2020–11695, 1717884, 692227. DOI: 10.2172/1717884. URL: https://www.osti.gov/servlets/purl/1717884/ (visited on 05/04/2023).

[48] Kelley Ruehl et al. *Experimental Testing of a Floating Oscillating Surge Wave Energy Converter*. en. Tech. rep. SAND–2019-3087, 1761877, 673585. Mar. 2019, SAND–2019–3087, 1761877, 673585. DOI: 10.2172/1761877. URL: https://www.osti.gov/servlets/purl/1761877/ (visited on 05/04/2023).

[49] V Heller. "PHYSICAL MODEL TESTS OF THE ANACONDA WAVE ENERGY CONVERTER". en. In: (2010).

[50] Aurélien Babarit et al. "Hydro-Elastic Modelling of an Electro-Active Wave Energy Converter". en. In: *Volume 9: Odd M. Faltinsen Honoring Symposium on Marine Hydrodynamics*. Nantes, France: American Society of Mechanical Engineers, June 2013, V009T12A033. ISBN: 978-0-7918-5543-0. DOI: 10.1115/OMAE2013-10848. URL: https://asmedigitalcollection.asme.org/OMAE/proceedings/OMAE2013/55430/Nantes,%20France/278461 (visited on 05/04/2023).

[51] Mohammad-Reza Alam. "A Flexible Seafloor Carpet for High-Performance Wave Energy Extraction". en. In: *Volume 4: Offshore Geotechnics; Ronald W. Yeung Honoring Symposium on Offshore and Ship Hydrodynamics*. Rio de Janeiro, Brazil: American Society of Mechanical Engineers, July 2012, pp. 839–846. ISBN: 978-0-7918-4491-5. DOI: 10.1115/OMAE2012-84034. URL: https://asmedigitalcollection.asme.org/OMAE/proceedings/OMAE2012/44915/839/269879 (visited on 05/15/2023).

[52] Marcus Lehmann et al. "The Wave Carpet: Development of a Submerged Pressure Differential Wave Energy Converter". en. In: (2014).

[53] AWS Ocean Energy Ltd. *Waveswing Wave Energy Converter Explained*. Apr. 2021. URL: https://www.youtube.com/watch?v=nrcLxxoEZos (visited on 06/01/2023).

[54] Richard Manasseh, Kathleen L McInnes, and Mark A Hemer. "Pioneering developments of marine renewable energy in Australia". en. In: *The International Journal of Ocean and Climate Systems* 8.1 (Apr. 2017), pp. 50–67. ISSN: 1759-3131, 1759-314X. DOI: 10.1177/1759313116684525. URL: http://journals.sagepub.com/doi/10.1177/1759313116684525 (visited on 05/04/2023).

[55] Gregory Poindexter. *CETO 5 marine energy system records 14,000 cumulative operating hours in Australia*. en-US. June 2016. URL: https://www.hydroreview.com/business-finance/business/ceto-5-marine-energy-system-records-14-000-cumulative-operating-hours-in-australia/ (visited on 06/01/2023).

[56] Marine Energy. *Carnegie Makes Wave Tech Headway*. en-US. Feb. 2020. URL: https://www.offshore-energy.biz/carnegie-makes-wave-tech-headway/ (visited on 06/01/2023).

[57] *Accomplishments Report Water Power Technologies Office FY22*. Tech. rep. 2022.

[58] Hangfei Li, Xiwen Sun, and Hui Zhou. "Wave energy: history, implementations, environmental impacts, and economics". en. In: *2nd International Conference on Materials Chemistry and Environmental Engineering (CONF-MCEE 2022)*. Ed. by Shuai Chen. ONLINE, United States: SPIE, Aug. 2022, p. 21. ISBN: 978-1-5106-5720-5 978-1-5106-5721-2. DOI: 10.1117/12.2646119. URL: https://www.spiedigitallibrary.org/conference-proceedings-of-spie/12326/2646119/Wave-energy-history-implementations-environmental-impacts-and-economics/10.1117/12.2646119.full (visited on 05/04/2023).

[59] Paolo Boccotti. "On a new wave energy absorber". en. In: *Ocean Engineering* 30.9 (June 2003), pp. 1191–1200. ISSN: 00298018. DOI: 10.1016/S0029-8018(02)00102-6. URL: https://linkinghub.elsevier.com/retrieve/pii/S0029801802001026 (visited on 05/17/2023).

[60] A. Babarit et al. "Investigation on the energy absorption performance of a fixed-bottom pressure-differential wave energy converter". en. In: *Applied Ocean Research* 65 (Apr. 2017), pp. 90–101. ISSN: 01411187. DOI: 10.1016/j.apor.2017.03.017. URL: https://linkinghub.elsevier.com/retrieve/pii/S0141118716303674 (visited on 05/04/2023).

[61] *Ocean Power: A Perfect Fit for Oregon*. en-US. June 2012. URL: https://www.corvallisadvocate.com/2012/ocean-power-a-perfect-fit-for-oregon/ (visited on 06/01/2023).

[62] Emiliano Renzi et al. "Niche Applications and Flexible Devices for Wave Energy Conversion: A Review". en. In: *Energies* 14.20 (Oct. 2021), p. 6537. ISSN: 1996-1073. DOI: 10.3390/en14206537. URL: https://www.mdpi.com/1996-1073/14/20/6537 (visited on 05/04/2023).

[63] Sandia National Labs. *FOSWEC Modeling and Control Design Testing*. Aug. 2020. URL: https://www.youtube.com/watch?v=OUxbaEC2K6Y (visited on 06/01/2023).

[64] *Langlee Technology | Langlee Wave Power*. URL: http://www.langleewp.com/?q=langlee-technology (visited on 05/24/2023).

[65] *Aquamarine Power : EMEC: European Marine Energy Centre*. URL: https://www.emec.org.uk/about-us/wave-clients/aquamarine-power/ (visited on 05/24/2023).

[66] *Waveroller*. en-US. URL: https://aw-energy.com/waveroller/ (visited on 05/24/2023).

[67] BPS Ocean Energy. *BPS | Ocean Energy*. en-AU. URL: https://bps.energy/ (visited on 05/24/2023).

[68] *Resolute Marine*. URL: http://www.resolutemarine.com/technology/ (visited on 05/24/2023).

[69] *Giant rubber snake could be the future of wave power | New Scientist*. URL: https://www.newscientist.com/article/dn14258-giant-rubber-snake-could-be-the-future-of-wave-power/ (visited on 06/01/2023).

[70] *SBM Offshore to Deploy WEC Prototype Off Monaco - Offshore Energy*. URL: https://www.offshore-energy.biz/sbm-offshore-to-deploy-wec-prototype-off-monaco/ (visited on 06/01/2023).

[71] Ye Li and Yi-Hsiang Yu. "A synthesis of numerical methods for modeling wave energy converter-point absorbers". en. In: *Renewable and Sustainable Energy Reviews* 16.6 (Aug. 2012), pp. 4352–4364. ISSN: 13640321. DOI: 10.1016/j.rser.2011.11.008. URL: https://linkinghub.elsevier.com/retrieve/pii/S1364032111005351 (visited on 05/04/2023).

[72] Nataliia Y Sergiienko et al. "Three-Tether Axisymmetric Wave Energy Converter: Estimation of Energy Delivery". en. In: (2016).

[73] Ashkan Rafiee and Jonathan Fievez. "Numerical Prediction of Extreme Loads on the CETO Wave Energy Converter". en. In: (2015).

[74] N.Y. Sergiienko et al. "An optimal arrangement of mooring lines for the three-tether submerged point-absorbing wave energy converter". en. In: *Renewable Energy* 93 (Aug. 2016), pp. 27–37. ISSN: 09601481. DOI: 10.1016/j.renene.2016.02.048. URL: https://linkinghub.elsevier.com/retrieve/pii/S0960148116301495 (visited on 05/04/2023).

[75] N.Y. Sergiienko et al. "Performance comparison of the floating and fully submerged quasi-point absorber wave energy converters". en. In: *Renewable Energy* 108 (Aug. 2017), pp. 425–437. ISSN: 09601481. DOI: 10.1016/j.renene.2017.03.002. URL: https://linkinghub.elsevier.com/retrieve/pii/S0960148117301829 (visited on 05/04/2023).

[76] N.Y. Sergiienko et al. "Feasibility study of the three-tether axisymmetric wave energy converter". en. In: *Ocean Engineering* 150 (Feb. 2018), pp. 221–233. ISSN: 00298018. DOI: 10.1016/j.oceaneng.2017.12.055. URL: https://linkinghub.elsevier.com/retrieve/pii/S002980181730793X (visited on 05/04/2023).

[77] Nataliia Y. Sergiienko et al. "Design Optimisation of a Multi-Mode Wave Energy Converter". en. In: *Volume 9: Ocean Renewable Energy*. Virtual, Online: American Society of Mechanical Engineers, Aug. 2020, V009T09A039. ISBN: 978-0-7918-8441-6. DOI: 10.1115/OMAE2020-19266. URL: https://asmedigitalcollection.asme.org/OMAE/proceedings/OMAE2020/84416/Virtual,%20Online/1093103 (visited on 05/04/2023).

[78] Mehdi Neshat et al. "A New Bi-Level Optimisation Framework for Optimising a Multi-Mode Wave Energy Converter Design: A Case Study for the Marettimo Island, Mediterranean Sea". en. In: *Energies* 13.20 (Oct. 2020), p. 5498. ISSN: 1996-1073. DOI: 10.3390/en13205498. URL: https://www.mdpi.com/1996-1073/13/20/5498 (visited on 05/04/2023).

[79] N. Tran et al. "Design considerations for a three-tethered point absorber wave energy converter with nonlinear coupling between hydrodynamic modes". en. In: *Ocean Engineering* 254 (June 2022), p. 111351. ISSN: 00298018. DOI: 10.1016/j.oceaneng.2022.111351. URL: https://linkinghub.elsevier.com/retrieve/pii/S0029801822007399 (visited on 05/04/2023).

[80] *ProteusDS Parts Library*. Apr. 2018. URL: https://dsaocean.com/downloads/beta-utilities/ProteusDSLibraryFilesv1.0.zip.

[81] *AMSTEEL-BLUE*. en. URL: https://www.samsonrope.com/energy/amsteel--blue (visited on 05/26/2023).

[82] Bingyong Guo and John V. Ringwood. "Geometric optimisation of wave energy conversion devices: A survey". en. In: *Applied Energy* 297 (Sept. 2021), p. 117100. ISSN: 03062619. DOI: 10.1016/j.apenergy.2021.117100. URL: https://linkinghub.elsevier.com/retrieve/pii/S0306261921005456 (visited on 05/04/2023).

[83] Gabrielle Dunkle, Shangyan Zou, and Bryson Robertson. "Wave Resource Assessments: Spatiotemporal Impacts of WEC Size and Wave Spectra on Power Conversion". en. In: *Energies* 15.3 (Feb. 2022), p. 1109. ISSN: 1996-1073. DOI: 10.3390/en15031109. URL: https://www.mdpi.com/1996-1073/15/3/1109 (visited on 05/08/2023).

[84] A. Babarit. "A database of capture width ratio of wave energy converters". en. In: *Renewable Energy* 80 (Aug. 2015), pp. 610–628. ISSN: 09601481. DOI: 10.1016/j.renene.2015.02.049. URL: https://linkinghub.elsevier.com/retrieve/pii/S0960148115001652 (visited on 05/05/2023).

[85] "Review and classification of wave energy converters". en. In: *Maritime Engineering and Technology* (Nov. 2012). Ed. by L. Pietra et al. DOI: 10.1201/b12726-82. URL: https://www.taylorfrancis.com/books/9780203105184/chapters/10.1201/b12726-82 (visited on 05/04/2023).

[86] Nataliia Y. Sergiienko et al. "Effect of a model predictive control on the design of a power take-off system for wave energy converters". en. In: *Applied Ocean Research* 115 (Oct. 2021), p. 102836. ISSN: 01411187. DOI: 10.1016/j.apor.2021.102836. URL: https://linkinghub.elsevier.com/retrieve/pii/S0141118721003084 (visited on 05/04/2023).

[87] Dunkle. “Wave Resource Assessments: Spacio-Temporal Effect of Wave Energy Converter Scale and Blue Economy Opportunities”. PhD thesis. Oregon State University, Sept. 2021.

Appendix A

ProteusDS Modeling Inputs

Float

RigidBodyCylinder Feature

// Added Mass Coefficients
$CaAxial 1
$CaNormal 1

// Dimensions
$Diameter 25
$Length 5

// Fluid loading
$WindLoading 0
$HydroLoading 1
$HydrostaticFroudeKrylov 2

// Mesh
$AxialSegments 5
$RadialSegments 3
$AngularSegments 30

// Soil loading
$SoilLoading 0

Input File

// Mass properties
$Ix 8.18e7
$Iy 8.18e7
$Iz 1.55e8
$Ixy 0
$Ixz 0
$Iyz 0
$DefineInertiaAboutCG 1
$CGPosition 0 0 0
$Mass 1.99e6

// Numerical
$Kinematic 0
$Cylinder float 0 0 0 0 0 0
$LinearQuadraticDrag rigidBodyLinear-
QuadraticDrag 0 0 0 0 0 0

Translator

RigidBodyCylinder Feature

```
// Dimensions
$Diameter 0.5
$Length 3

// Fluid loading
$WindLoading 0
$HydroLoading 0
$HydrostaticFroudeKrylov 0

// Mesh
$AxialSegments 2
$RadialSegments 2
$AngularSegments 8

// Soil loading
$SoilLoading 0
```

Input File

```
// Mass properties
$Ix 1
$Iy 1
$Iz 1
$Ixy 0
$Ixz 0
$Iyz 0
$DefineInertiaAboutCG 1
$CGPosition 0 0 0
$Mass 100

// Numerical
$Kinematic 0
$Cylinder translator 0 0 0 0 0 0
```

Casing

RigidBodyCylinder Feature

```
// Dimensions
$Diameter 1
$Length 6

// Fluid loading
$WindLoading 0
$HydroLoading 0
$HydrostaticFroudeKrylov 0

// Mesh
$AxialSegments 2
$RadialSegments 2
$AngularSegments 8

// Soil loading
$SoilLoading 0
```

Input File

```
// Mass properties
$Ix 1
$Iy 1
$Iz 1
$Ixy 0
$Ixz 0
$Iyz 0
$DefineInertiaAboutCG 1
$CGPosition 0 0 0
$Mass 100

// Numerical
$Kinematic 0
$Cylinder casing 0 0 0 0 0 0
```

Anchor

RigidBodyCylinder Feature

```
// Dimensions
$Diameter 1
$Length 1

// Fluid loading
$WindLoading 0
$HydroLoading 0
$HydrostaticFroudeKrylov 0

// Mesh
$AxialSegments 2
$RadialSegments 2
$AngularSegments 4

// Soil loading
$SoilLoading 0
```

Input File

```
// Mass properties
$Ix 1
$Iy 1
$Iz 1
$Ixy 0
$Ixz 0
$Iyz 0
$DefineInertiaAboutCG 0
$CGPosition 0 0 0
$Mass 100

// Numerical
$Kinematic 1
$Cylinder anchor 0 0 0 0 0 0
```

PTO Joint

RigidBodyABAConnection

```
// End stop settings
$EJoint 3.5
$E0Joint 0

// End stop stiffness and damping
$KEJoint 1e8
$CEJoint 0

// Joint stiffness and damping
$KJoint *Set IAW configuration
$CJoint *Set IAW configuration
```

Connection

```
Master: casing1-5
Follower: translator1-5

// Mechanical
$MasterConnectionLocation 0 0 1 0 0 0
$FollowerConnectionLocation 0 0 0 0 0 0
$Joint 0
$FollowerJointAxis 2

// Uncategorized properties
$PrismaticJointLinear ptoJoint
```

Anchor Joint

RigidBodyABAConnection

// End stop settings
$EJoint 0
$E0Joint 0

// End stop stiffness and damping
$KEJoint 0
$CEJoint 0

// Joint stiffness and damping
$KJoint 0
$CJoint 0

Connection

Master: anchor1-5
Follower: casing1-5

// Mechanical
$MasterConnectionLocation 0 0 0 0 0 0
$FollowerConnectionLocation 0 0 3 0 0 0
$Joint 4

// Uncategorized properties
$SphericalJointAngular0 anchorJoint
$SphericalJointAngular1 anchorJoint
$SphericalJointAngular2 anchorJoint

Tether

Node 0 Connection

Master: float
Follower: tether1-5

// Mechanical
$DCableFollowerNodeN 0
$DCableFollowerLocation X Y Z

Input File

// Boundary constraints
$Node0Static 0
$NodeNStatic 0

// Fluid loading
$FluidLoadingMode 0

// Mechanical
$CableSegmentMode 1

Node N Connection

Master: translator1-5
Follower: tether1-5

// Mechanical
$DCableFollowerNodeN 1
$DCableFollowerLocation 0 0 -2.5

Configuration Dependent Inputs

The initial positions of the float, casings, anchors, and tether nodes depend on the configuration. These are calculated using the MATLAB ProteusDS Geometry Script contained

in 8. These values are captured in the data files of these DObjects, and the tether node 0 connection locations on the float.

Appendix B

MATLAB Configuration Geometry Script

Figures 1 and 2 depict the trigonometry used to calculate the positions of the different components of the WEC device, including the float, anchor, and tether nodes, using the three-tether configuration as an example. The MATLAB script used for calculations is provided below.

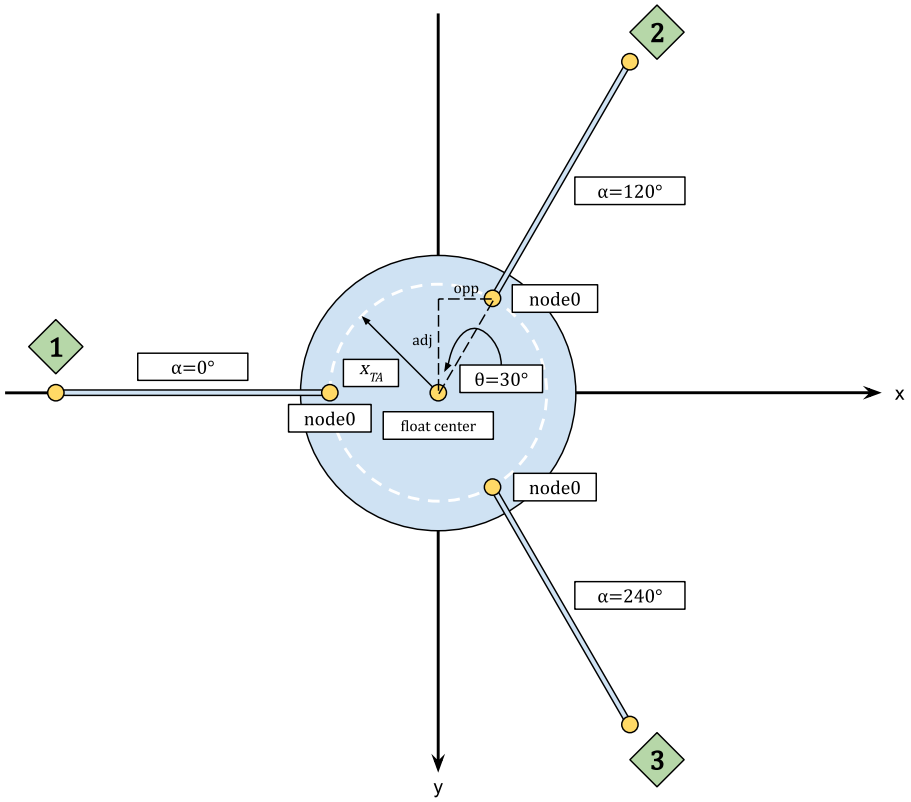

Figure 1: Top view diagram used for geometry calculations (three-tether example).

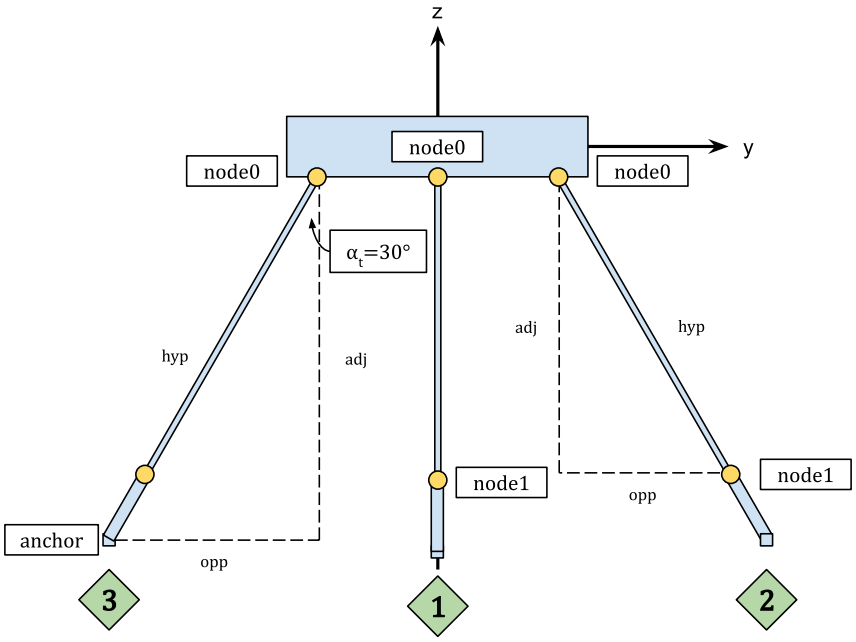

Figure 2: Side view diagram used for geometry calculations (three-tether example).

ProteusDS Geometry Script

```
clear all
clc
```

Configuration Parameters

```
numOfTethers = 3;
h = 100; % water depth [m]
ds = 6.5; % depth of submergence (from top of the float) [m]
H = 5; % floatHeight [m]
casingL = 6; % length of the casing [m]
anchorH = 1; % height of the anchor [m]
x_TA = 10; % tether attachement point distance from center of the float [m]
a_t = 30; % tether inclination angle [deg]
degOfSep = 360 / numOfTethers; % degrees of separation between tethers [deg]

% offset for equilibrium setup [m]
z_offset = 1; % [m]
if numOfTethers ~= 1
    z_offset = sind(90-a_t)*z_offset; % z-axis offset [m]
end

% Float Inital Position
floatPOS = [0 0 ds+H/2+z_offset]; % float inital position [X,Y,Z]

% Alpha values for each tether
for i=1:numOfTethers
    a(i) = degOfSep*(i-1);
end

% Tether node0 values
for i=1:numOfTethers
    x0(i) = cosd(a(i))*x_TA;
    y0(i) = sind(a(i))*x_TA;
end

% Tether Node0 Z-Coordinate
z_0 = ds+H+z_offset; % z-coord of all node0 tethers
```

Anchor-to-TetherNode0 Trigonometry

```
% Side View Calcs
z_anchor = h - anchorH/2; % z-coord of all anchors
anchor2tetherNode0Adj = z_anchor - z_0; % vertical distance betweeen anchor & node0
anchor2tetherNode0Hpy = anchor2tetherNode0Adj / cosd(a_t); % distance between anchor & node0
anchor2tetherNode0Opp = tand(a_t)*anchor2tetherNode0Adj; % horizontal distance between anchor & node0

anchor2tetherNode0 = x_TA+anchor2tetherNode0Opp; % total distance between anchor and tether node0

% coordinate for the anchor
for i=1:numOfTethers
    x_anchor(i) = cosd(a(i))*anchor2tetherNode0;
    y_anchor(i) = sind(a(i))*anchor2tetherNode0;
end
```

TetherNode0-to-TetherNode1 Trigonometry

```
% Side View Calcs
tetherNode02tetherNode1Hpy = anchor2tetherNode0Hpy - casingL; % distance between node0 & node1
tetherNode02tetherNode1Adj = tetherNode02tetherNode1Hpy*cosd(a_t); % vertical distance between node0 & node1
tetherNode02tetherNode1Opp = tetherNode02tetherNode1Hpy*sind(a_t); % horizontal distance between node0 & node1
```

```
tetherNode02tetherNode1 = x_TA+tetherNode02tetherNode1Opp; % total distance between tether node0 and node1
z_1 = z_0+tetherNode02tetherNode1Adj; % z-coord for all tether node1's


for i=1:numOfTethers
    x1(i) = cosd(a(i))*tetherNode02tetherNode1;
    y1(i) = sind(a(i))*tetherNode02tetherNode1;
end
```

ProteusDS Inputs

Initial position of the float based on the depth of submergence, height of the float and the z-offset needed to allow the translator to achieve equilibrium.

```
floatPOS
```

```
floatPOS = 1×3
         0         0    9.8660
```

Initial position of anchors and tethers, reported in (x,y,z) coordinates. Tethers include two sets of values, the first corresponds to the node0 location, and the second is the nodeN location.

```
if numOfTethers == 1
    anchor1 = [0 0 z_anchor]
    tether1 = [0 0 z_0; ...
               0 0 z_anchor-casingL]


elseif numOfTethers == 3
     anchor1 = [-x_anchor(1) y_anchor(1) z_anchor]
     anchor2 = [-x_anchor(2) y_anchor(2) z_anchor]
     anchor3 = [-x_anchor(3) y_anchor(3) z_anchor]
     tether1 = [-x0(1) y0(1) z_0;...
                -x1(1) y1(1) z_1]
     tether2 = [-x0(2) y0(2) z_0;...
                -x1(2) y1(2) z_1]
     tether3 = [-x0(3) y0(3) z_0;...
                -x1(3) y1(3) z_1]


elseif numOfTethers == 4
     anchor1 = [-x_anchor(1) y_anchor(1) z_anchor]
     anchor2 = [-x_anchor(2) y_anchor(2) z_anchor]
     anchor3 = [-x_anchor(3) y_anchor(3) z_anchor]
     anchor4 = [-x_anchor(4) y_anchor(4) z_anchor]
     tether1 = [-x0(1) y0(1) z_0;...
                -x1(1) y1(1) z_1]
     tether2 = [-x0(2) y0(2) z_0;...
                -x1(2) y1(2) z_1]
     tether3 = [-x0(3) y0(3) z_0;...
                -x1(3) y1(3) z_1]
     tether4 = [-x0(4) y0(4) z_0;...
                -x1(4) y1(4) z_1]

elseif numOfTethers == 5
     anchor1 = [-x_anchor(1) y_anchor(1) z_anchor]
     anchor2 = [-x_anchor(2) y_anchor(2) z_anchor]
     anchor3 = [-x_anchor(3) y_anchor(3) z_anchor]
     anchor4 = [-x_anchor(4) y_anchor(4) z_anchor]
     anchor5 = [-x_anchor(5) y_anchor(5) z_anchor]
     tether1 = [-x0(1) y0(1) z_0;...
                -x1(1) y1(1) z_1]
     tether2 = [-x0(2) y0(2) z_0;...
                -x1(2) y1(2) z_1]
```

```
    tether3 = [-x0(3) y0(3) z_0;...
               -x1(3) y1(3) z_1]
    tether4 = [-x0(4) y0(4) z_0;...
               -x1(4) y1(4) z_1]
    tether5 = [-x0(5) y0(5) z_0;...
               -x1(5) y1(5) z_1]

end
```

```
anchor1 = 1×3
  -60.3068         0   99.5000
anchor2 = 1×3
   30.1534   52.2272   99.5000
anchor3 = 1×3
   30.1534  -52.2272   99.5000
tether1 = 2×3
  -10.0000         0   12.3660
  -57.3068         0   94.3038
tether2 = 2×3
    5.0000    8.6603   12.3660
   28.6534   49.6292   94.3038
tether3 = 2×3
    5.0000   -8.6603   12.3660
   28.6534  -49.6292   94.3038
```